Modelling and 3D simulation of ductile crack growth with non-local Gurson-based formulation

Thomas Pardoen[a,b], Antonio Kaniadakis[a], Van-Dung Nguyen[a,c], Ludovic Noels[c], Sara Javangorough[a], Jacques Besson[d]

[a]*Institute of Mechanics, Materials and Civil Engineering, UCLouvain, Place Sainte Barbe 2, Louvain la Neuve, B-1348, Belgium*
[b]*WEL Research Institute, Avenue Pasteur 6, Wavre, B-1300, Belgium*
[c]*Computational & Multiscale Mechanics of Materials, Department of Aerospace and Mechanical Engineering, University of Liège, Belgium, Allée de la découverte 9, Liège, B-4000, Belgium*
[d] *Mines Paris, PSL Research University, Centre des Matériaux, CNRS UMR 7633, 63-65 rue Henri-Auguste Desbruères, Corbeil-Essonnes, 91003, France*

Abstract

The state of maturity of the micromechanics of ductile fracture is such that it is possible, today, to simulate extensive crack growth in 3D using a sophisticated physics-based description of the mechanisms of nucleation, growth and coalescence of voids within a non-local formulation. Here, different phenomena related to ductile crack growth are addressed in the context of fracture mechanics specimens. Structural integrity assessments of many critical components rely indeed on predictive models of crack growth from pre-existing sharp defects. Two similar extended Gurson models are used, after comparison to cross-verify their numerical implementation, to generate results about the effect of plate thickness, plastic anisotropy and strain hardening. The variation of the fracture toughness increasing and then decreasing with thickness down to the plane strain regime is captured owing to the 3D nature of the simulations, capturing the crack tip necking phenomenon. The non-local formulation introduces a length scale that sets the range over which the fracture toughness depends on thickness. The thickness effect disappears when using homothetic geometries. The effect of plasticity anisotropy is shown to be particularly important when a crack grows in sheets exhibiting significant crack tip necking through increasing or not the plastic dissipation in the neck. A large strain hardening capacity enhances very much the fracture toughness, an effect that is amplified in 3D when crack tip necking takes place. These findings constitute only a limited set of answers to many remaining questions in the very important field of ductile tearing, setting an ambitious roadmap for the years to come to the solid mechanics community. These questions are particularly important in the context of modern technologies such as H_2 storage, additive manufacturing, new high strength metallic alloys development, and generation IV nuclear fission and fusion reactors to name a few.

Keywords: Ductile Failure, Fracture toughness, J-integral, Strain hardening, Void growth

*Corresponding author
Email address: thomas.pardoen@uclouvain.be (Thomas Pardoen)

1. Introduction

Ductile fracture has received continuous attention from the mechanical and materials engineering community for more than 60 years, see for instance reviews of Benzerga and Leblond (2010), Pineau et al. (2016). Still, the subject keeps rejuvenating decades after decades motivated by novel challenges and problems set by technological progress. Today, the focus is among others on (i) the development of novel metallic alloys with excellent fracture toughness such as TWIP/TRIP steels or titanium and high entropy alloys that can be used with thinner sections affecting the crack growth process, e.g. Gludovatz et al. (2016), Choisez et al. (2020), Ismail et al. (2021), (ii) the production of ultra-high strength alloys which suffer from competitions between different failure modes, e.g. Frómeta et al. (2021), Xiong et al. (2018), (iii) H_2 storage and transport with questions on the embrittlement of nominally ductile metals, e.g. Lopes Pinto et al. (2024), (iv) nuclear applications for generation IV fission and fusion reactors as well as for long term operation beyond 60 years of the current fleet which leads to novel questions associated to the high irradiation doses and /or embrittlement and/or temperature effects, e.g. Zinkle and Busby (2009), Yin et al. (2021); (v) the deployment of metal additive manufacturing that show sometimes unsatisfactory ductility and toughness, e.g. Das (2022). In all these problems, linking the mechanical integrity analysis to the micromechanics and physics of the ductile failure process and microstructure appears as the most convincing science-based approach to support the technology development. One of the core questions always remains: how to transfer the laboratory scale mechanical testing measurements, in particular when using miniaturized fracture mechanics tests, to real structures in a conservative manner through predictive models?

The solid mechanics community interested by micromechanics-based approaches has always been working hand by hand with metallurgists to characterize, understand and model ductile fracture in metals. Although the initial focus was, typically in the 80's and 90's, to predict the fracture toughness and tearing resistance in a fracture mechanics context, the attention has then switched very much towards developing finer and finer description of the damage process. As a result, the state of maturity regarding the modeling of the mechanisms of nucleation, growth and coalescence of voids is today quite high. In particular, the Gurson model (Gurson, 1977) and its evolutions often based on the Gurson-Tvergaard-Needleman (GTN) extension (Tvergaard and Needleman, 1984) has been the workhorse in the field. But, most of the time, the focus is on the prediction of the fracture strain under different loading conditions, while studies addressing the fracture toughness and resistance to crack growth in real fracture mechanics specimens and components remain rare. The main reason is probably that dealing with long crack extensions is more complicated than addressing homogeneous or near-homogeneous loadings. In particular, one of the main difficulty is that models that embed the possibility of material strain softening, such as the GTN model, show a loss of ellipticity of the governing equations resulting in strain localization in band with thickness that depends on mesh size. The boundary value problem gets ill-posed with results that depend on mesh density (De Borst et al., 1993). The remedy that was used in early studies dealing with crack growth simulations using Gurson-type models was to consider the size of the finite element mesh as an additional material parameter (e.g. Xia (1995)). But this is an artificial solution, creating, among others, problems of transferability when dealing with different geometries. Cohesive zone models solve the problem by introducing a length scale but at the

cost of making the description of the failure process insensitive to the stress state (in particular the local stress triaxiality level at the crack tip; for cohesive models that take stress triaxiality into account, refer to Siegmund and Brocks (2000) and Tvergaard (2001), however, such an enhancement is somewhat phenomenological and reintroduces the problem of mesh dependency.) The most convincing solution is to develop non-local formulations that introduce a physical length scale associated to the damage process. This has been an important subject of research for about three decades.

Non-local formulations of damage models introduce one or several intrinsic lengths into the constitutive relationships (Bažant and Jirásek (2002); Jirásek (1998); Peerlings et al. (2001)). This assumes the dependence of the damage indicator on one or multiple non-local variables which, in the computational method, can be estimated by volume averaging over a characteristic volume of their local counterparts or through the computation of the gradients of the variables. Non-local extensions (often of the Gurson-based model) may be divided into three different categories: (i) integral type, see e.g. the early works by Leblond et al. (1994), Tvergaard and Needleman (1995), (ii) explicit gradient type, see e.g. models by Chen and Yuan (2002), (iii) simplified strain gradient plasticity based on a scalar variable Zhang et al. (2018), and (iv) implicit gradient type, see e.g. developments by Ramaswamy and Aravas (1998), Reusch et al. (2003b), Reusch et al. (2003a), Håkansson et al. (2006), Linse et al. (2012), Hütter et al. (2013a), Hütter et al. (2013b), Zybell et al. (2014), and Tuhami et al. (2022). The implicit gradient is more easily integrated into standard finite element procedures compared to the integral type (Peerlings et al., 1996). In the implicit gradient type, either the porosity (Håkansson et al. (2006); Ramaswamy and Aravas (1998)), the effective porosity (Reusch et al. (2008); Reusch et al. (2003a,b)), or the volumetric equivalent plastic strain (Hütter et al. (2013a,b); Linse et al. (2012); Zybell et al. (2014)) is generally chosen as a non-local variable. These non-local formulations have proved effective for regularizing the problem of mesh sensitivity. However, they often rely on a simplified description of the nucleation, growth and coalescence process. Up to now, engineering fracture mechanics problems including 3D crack growth in full specimens or components have rarely been addressed with such non-local models, and especially with advanced GTN-type models. The first goal of the paper is to show that such a sophisticated formulation, as presented in Section 2, can be used to simulate 3D problems with acceptable computer resources. Two different codes relying on similar advanced non-local GTN model (Tuhami et al. (2022); Nguyen et al. (2020)) will be used for this purpose, after a comparison of their predictions on a representative crack growth problem given in Appendix C.

With such reliable computational models available, it is possible today to reinvestigate a number of important questions related to ductile crack growth and sometimes to look at questions never fully solved in the literature up to now such as: what is the origin of the thickness effect on the ductile fracture toughness and can we predict it throughout the entire range ? What is the importance of plastic anisotropy on the fracture toughness of ductile metals, especially in the context of thin metal sheet exhibiting severe crack tip necking ? What is the impact of the strain hardening capacity which is today of much interest in metallic alloys design? How can we link the different fracture resistance indicators proposed in the literature for the initiation and propagation of cracks such as the critical value of the J-integral at initiation J_c or after a given amount of crack growth (for instance equal to 0.2mm) $J_{0.2}$, the critical crack tip opening displacement δ_c, the tearing modulus T_J and the crack tip opening angle during propagation CTOA? What are the parameters

that control the flat versus slant fracture transition? How to model failure mode transitions ductile transgranular to ductile intergranular, ductile versus cleavage transgranular, ductile versus cleavage intergranular? Although it is impossible to cover all these questions within a single study, the second goal of the paper is to provide novel results at least regarding the three first questions, sequentially in Sections 4, 5 and 6, touching also partly to the fourth one. Before that, Section 3 provides few representative results for 3D cracked specimens to remind some of the key features of ductile crack growth with 3D effects, in order set the stage for the next sections and explain how the results are extracted from the simulations.

The analysis will be limited to two specific fracture mechanics test configurations shown in Fig. 1: the Compact Tension geometry (CT), which is the mostly used fracture mechanics geometry, and the Double Edge Notched Tension geometry (DENT) owing to its simplicity but also its versatility being the preferred choice for thin plate fracture. There will be no direct comparison with experiments but it is important to indicate that the non-local models used in this study have been validated in recent years through comparisons with experimental programs, e.g. Hilhorst et al. (2022). As explained above, the focus is limited to precracked geometries and not on predicting the fracture strain for a range of loading conditions, which has been the purpose of many former studies in the literature, including from the authors of the present paper. Different hardening laws and damage parameters will be addressed. The results, more than putting a final answer to the questions listed above, will show the need to push the investigation further in many directions, also opening other unexpected interrogations. The ultimate ambition of this paper is to show that there are still major progress and outstanding issues for the field of ductile fracture in the context of predicting crack growth, as recapitulated in the conclusion and perspectives to set a roadmap for the years to come.

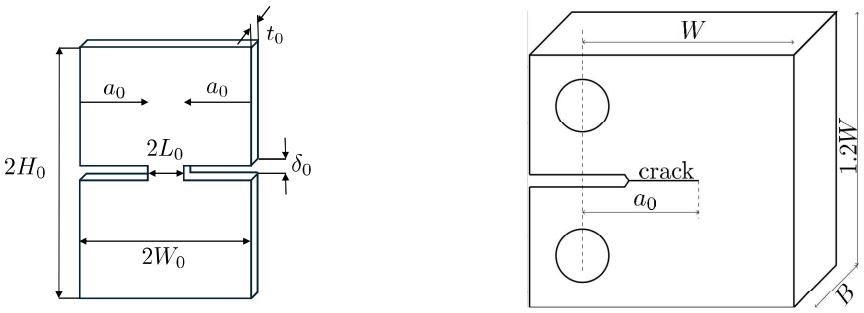

Figure 1: Sketch of the geometry of the DENT and CT specimen considered in the present study.

2. Description of the models

2.1. Non-local GTN models and numerical methods

Although several other damage models have been developed in the mechanics of materials / solid mechanics literature, the Gurson model has received the largest attention and is the most widely

used. Today, following the steps of Tvergaard and Needleman (1984), the Gurson model has been fine tuned to be more accurate when dealing with different hardening characteristics (Faleskog et al., 1998), extended to void coalescence in different ways (Benzerga (2002); Pardoen and Hutchinson (2000)), to void nucleation (Chu and Needleman (1980) and later for instance by Marteleur et al. (2021)), to plastic anisotropy (Benzerga and Besson (2001)), to void shape effects (Gologanu et al., 1993), and to shear distortion effects (Nahshon and Hutchinson, 2008). The ingredients of the two formulations and models used in this study are summarized in the comparative Table 1, indicating also the extra available ingredients that were not activated in this specific study. In particular, shear effects on void growth and on void coalescence are not activated as justified by the flat mode I nature of the crack problems addressed in this study. The goal when making these choices was to allow comparing the two computational models under almost exactly similar assumptions and equations for the cross-validation exercise presented in Appendix C. This justifies that the results presented hereafter have been generated indistinctly with the two codes considering that the goal is essentially to discuss relative effects. The main equations of the models are given in Appendix A but all details are not repeated as they have been presented at length in earlier papers (Nguyen et al. (2020); Tuhami et al. (2022)).

2.2. *Material parameters*

The Swift hardening law is used for all simulations as defined by

$$\sigma_Y = \sigma_0 \left(1 + k_k \varepsilon_m\right)^n , \tag{1}$$

where σ_Y is the current yield stress, σ_0 is the initial yield stress, ε_m the accumulated matrix plastic strain, k_k is a hardening parameter and n is the strain hardening exponent. Elasticity is linear isotropic with Young's modulus E and Poisson ratio ν always taken equal to 0.3. The other material parameters that are varied are the initial porosity f_0, as well as the Lankford coefficient r_L to address plastic anisotropy in transversely isotropic materials in Section 5 as defined by

$$r_L = \frac{\Delta\varepsilon_{yy}}{\Delta\varepsilon_{zz}}. \tag{2}$$

Table 2 gathers the list of material parameters used in this study.

Two different values of initial porosity f_0 equal to 0.01 and 0.001 are considered, with a void distribution ratio λ_0 equal to 1. The non-local length l_{nl} is set equal to 100 μm. As explained in Kaniadakis et al. (2025), such l_{nl} value would correspond to a void spacing of typically 300 μm which is at the upper bound of what is typically found in metallic alloys, often showing quite smaller void spacings. In case the model would be used to analyze and compare to experimental results, the length l_{nl} would be one of the few parameters to be calibrated by inverse modelling in order to capture the right magnitude of the dissipation during cracking. Before any simulation is run, the q_1 and q_2 parameters of the Gurson model are fine-tuned as a function of the hardening parameters and of f_0 using void cell simulations as further explained in Appendix B. A_n is the void nucleation intensity function, here set to zero (hence no extra porosity is generated beyond the initial one). Also, the coalescence parameters, either κ, α and β are adjusted using the same

Table 1: Comparison of non-local Gurson models and formulations.

	Non-local Gurson Model 1	Non-local Gurson Model 2
Reference	Nguyen et al. (2020)	Tuhami et al. (2022)
Yield surface for void growth	GTN isotropic and anisotropic version (see Section 5 for more info on the anisotropy)	GTN isotropic and anisotropic version
Porosity growth law	$\dot{f} = (1-f)\,\mathrm{tr}(\mathbf{D}^p)$ + shear (shear not activated here)	$\dot{f} = (1-f)\,\mathrm{tr}(\mathbf{D}^p)$
Void coalescence by internal necking	Thomason-based yield surface	Critical porosity followed by acceleration factor (fitted to match with Thomason-based coalescence predictions)
Void coalescence under shear	Shear coalescence yield surface (not activated here)	not available
Non-local variables	3 variables $\bar{\varepsilon}_v$, $\bar{\varepsilon}_m$, $\bar{\varepsilon}_d$ (volumetric, matrix, deviatoric plastic strain) - only one activated here	2 variables $\bar{\varepsilon}_v$, $\bar{\varepsilon}_m$ (volumetric and matrix plastic strain) - only one activated here
Void nucleation	Chu and Needleman (1980), Marteleur et al. (2021)	Chu and Needleman (1980), Zhang et al. (2000), or any possible void nucleation function
Particularities	Three-yield surface model integrated into one	single yield surface
Finite strain formulation	Corotational formulation	Corotational formulation
Elements	Quadratic tetrahedra with fully implicit integration	Linear hexahedra with full integration and F-bar formulation (Elguedj et al., 2008)
Hardening law	Rate independent	Rate independent (rate dependent version also available)

Table 2: Material parameters used in the simulations.

Elastoplastic parameters	$E = 200$ GPa, $\nu = 0.3$, $\sigma_0 = 300$ MPa, $k_k = 666$, $n = 0.1, 0.3, 0.5$
Porosity characteristics	$f_0 = 10^{-3}, 10^{-2}$, $\lambda_0 = 1$, $A_n = 0$,
Adjusting parameters	$q_1(n, f_0)$, $q_2(n, f_0)$, $\kappa(n, f_0)$, $\alpha(n, f_0)$, $\beta(n, f_0)$
Non-local parameters	$l_{nl} = 100\,\mu$m

void cell simulations for the Code 1 (Nguyen et al., 2020) and the critical porosity at the onset of coalescence f_c and the critical porosity at fracture f_R for the Code 2 (Tuhami et al., 2022) for $n = 0.1$. These two critical values of porosity were computed with Code 1, considering the loading path of a material point at distance $X = l_{nl}$ from the crack tip in order to set a good correspondence between the two models. Table 3 gathers the q_1, q_2, κ, α, and β parameters identified on axisymmetric void cell calculations. These parameters are used in Section 3, 4, 6, while in Section 5 these parameters will also be adjusted as a function of the plastic anisotropy.

Table 3: GTN-coalescence parameters used in the simulations. Note that Code 2 has not been used for calculations with $n = 0.3$ and $n = 0.5$.

					Code 1		Code 2	
f_0	n	q_1	q_2	κ	α	β	f_c	f_R
10^{-3}	0.5	1.111	0.928	1.487	0.017	1.909	-	-
10^{-2}	0.5	1.559	0.821	1.481	0.073	1.798	-	-
10^{-3}	0.3	1.103	0.966	1.496	0.286	1.551	-	-
10^{-2}	0.3	1.161	0.949	1.487	0.353	1.520	-	-
10^{-3}	0.1	1.317	0.993	1.492	0.320	1.185	0.03	0.08
10^{-2}	0.1	1.018	1.067	1.147	0.366	1.195	0.05	0.12

2.3. FE models for the cracked specimens

As mentioned above and shown in Fig. 1, CT and DENT specimens are simulated with characteristic dimensions t_0, W_0, L_0, H_0, and B_0. The initial crack tip opening displacement δ_0 is systematically selected small enough to ensure that it is much smaller than the critical value δ_c. In this case, δ_0 is not a parameter of the problem as it should not influence the solution. This condition is needed to guarantee that the starter crack is indeed sufficiently sharp to be a valid precrack in the sense of fracture mechanics.

The FE meshes are shown in Fig. 2. The number of elements in the thickness is selected large enough through convergence analysis to capture the gradients that develop from the midplane to the surface. The meshes are relatively coarse in areas far from the initial crack tip, while a finer mesh is employed along the direction of crack propagation. Specifically, the element size l_e in the ligament direction is always equal to 1/3 of the non-local length l_{nl}.

The J value for the DENT specimen is calculated using Rice's formula (Rice et al., 1973)

$$J_{\text{DENT}} = J_e + J_p = \frac{K_I^2}{E} + \frac{1}{L_0 t_0}\left[2\left(\int_0^{u_p} F(u_p')du_p'\right) - Fu_p\right], \tag{3}$$

with J_e and J_p the elastic and plastic contribution of the J-integral respectively, K_I the stress intensity factor, F the force, u_p the plastic displacement at which J_p is calculated. The expression of K_I reads

$$K_I = \Sigma\sqrt{\pi a_0} f(a_W), \tag{4}$$

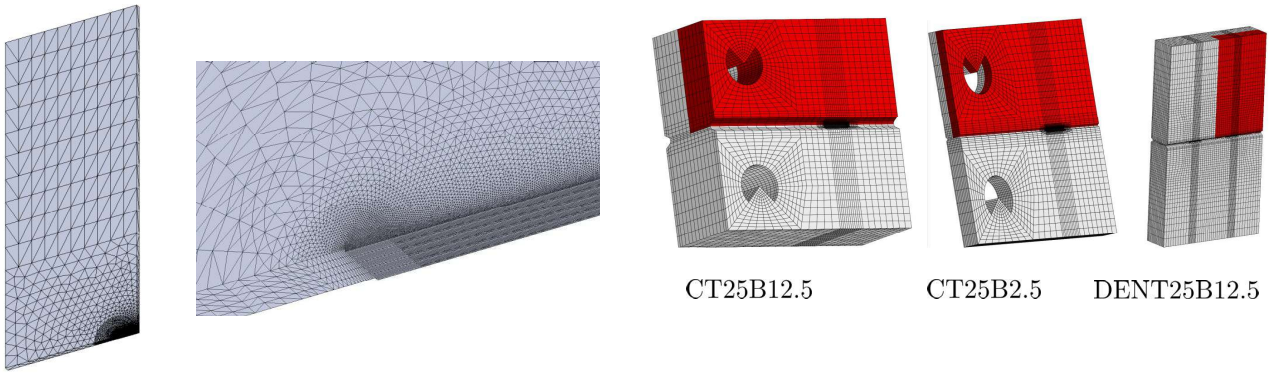

a) b)

Figure 2: Finite element meshes for the DENT and CT specimen in the outer region and in the region close to the initial crack tip. The red part is the region considered for the simulations owing to symmetry. a) Mesh with quadratic tetrahedra employed in Code 1; b) Mesh with linear hexahedra employed in Code 2.

with

$$a_0 = W_0 - L_0, \qquad a_W = \frac{a_0}{W_0}. \tag{5}$$

The geometrical correction factor $f(a_W)$ reads

$$f(a_W) = \frac{1.122 - 0.561a_W - 0.205a_W^2 + 0.471a_W^3 - 0.19a_W^4}{\sqrt{1 - a_W}}, \tag{6}$$

and the quantity Σ is defined as

$$\Sigma = \frac{F}{2W_0t_0}. \tag{7}$$

Fig. 3 shows that the J value calculated near the instant of cracking initiation using the direct contour integral definition based on the FE solution is close to the J value obtained from Rice's formula (using a typical simulation as described later in the paper). This validates the accuracy of Rice's formula.

For the CT specimens, all simulations are post-processed to extract the J-integral and the crack growth by applying the methodology described in the ASTM E1820 standard. The crack extension is determined by mimicking the experimental procedure. The J-integral is $J = J_e + J_p$, with the plastic part that is incrementally computed as in Ernst et al. (1981):

$$J_p^k = J_p^{k-1} + \left(\frac{\eta_p^{k-1}}{b^{k-1}B_N}\left(A_p^k - A_p^{k-1}\right)\right) \times \left(1 + \frac{\gamma_p^{k-1}}{b^{k-1}}\left(a^k - a^{k-1}\right)\right), \tag{8}$$

where k represents the current load step. Note that in actual tests, k corresponds to an instant at which the crack length is measured. This measure can be performed experimentally using the

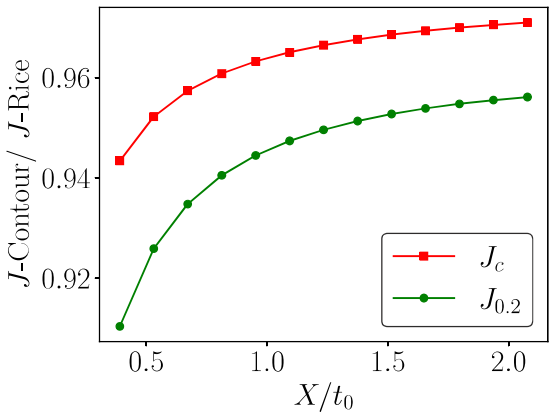

Figure 3: Comparison between the value of J computed on several contours characterized by a certain size X/t_0 and the value of J computed using Rice's formula. The red line represents the critical value at crack onset J_c, while the green line the value computed after a crack growth of 0.2 mm.

potential drop method or the elastic unloading method. a is the crack length, and b is the specimen ligament size ($b = W - a$). A_p is the area under the load—plastic displacement curve, and η_p is the plastic correction factor

$$\eta_p = 2 + 0.552\frac{b}{W}, \qquad \gamma_p = 1 + 0.76\frac{b}{W}. \tag{9}$$

The expression of the compliance from ASTM E1820 is required to evaluate the plastic part of the displacement.

2.4. Dimensional analysis

Dimensional analysis shows that J_c (here for DENT specimen) depends on the following parameters

$$J_c = \sigma_0 l_{nl} F\left(\frac{\sigma_0}{E}, n, \nu, r_L, f_0, \frac{l_{nl}}{t_0}, \frac{W_0}{t_0}, \frac{L_0}{W_0}\right), \tag{10}$$

in which we have not introduced the parameters λ_0 taken equal to 1 (isotropic distribution), χ_0 directly derived from $\chi_0 = (1.5\lambda_0 f_0)^{1/3}$, and the void nucleation parameters (voids are taken to be initially present). The focus in this paper will be essentially on the impact of n, f_0, r_L, l_{nl}/t_0 and W_0/t_0 on J_c and on crack growth resistance indicators such as the degree of crack tip necking and on the critical crack tip opening displacement δ_c. δ_c can be extracted from the FE simulation directly or obtained from Shih formula:

$$\delta_c = d_n \frac{J_c}{\sigma_0}, \tag{11}$$

in which d_n is the so-called Shih parameter, tabulated for plane stress and plane strain conditions as a function of n.

3. Generic representative results

Code 1 has been used to generate a first set of representative results for a standard simulation of a DENT specimen characterized by $n = 0.1$, $f_0 = 10^{-2}$, $t_0 = 2$mm, and $l_{nl} = 100\mu$m. As shown in Appendix C, the two codes provide very similar results when used to simulate this complex problem. Fig. 4 presents different key results regarding the overall and local fields. Fig. 4 a) gives the J_R curve in which J value is normalized by the initial yield stress σ_0 and by the nonlocal length l_{nl}. Cracking initiation takes place at a normalized value equal to 5.7, easily detected by the marked change of slope. The points on the J_R curve denote the values of J considered for the following figures. Fig. 4 b) shows the variations of the opening stress along the center plane as a function of the distance to the crack tip X normalized by the thickness, for different J values. Various steps that led to the same crack advance increment were considered. The peak value of the opening stress associated to the first three J values (which are below J_c) are lower than those found during crack growth. This phenomenon can be attributed to the blunting of the crack tip. As the crack advances, the peak opening stress keeps increasing and eventually stabilizes at a constant value that is independent of J. This behavior has been previously reported for instance in Chen et al. (2020). It is important in the context of the ductile brittle transition very much driven by the magnitude of the maximum principal stress (see also Xia and Shih (1996), Petti and Dodds (2005)). This explains, for instance, why the probability for a ductile crack to transition into cleavage increases as the crack grows.

Turning to the stress triaxiality depicted in Fig. 4 c) again along the center plane, the peak decreases until crack initiation as a result of the crack blunting process, after which it increases again just after initiation before gradually decreasing with increasing J. Note that the values of the stress triaxiality around 1.5 are much lower than the small scale yielding values (around 3 times), due to the loss of constraint associated to the limited thickness and the near plane stress regime. Fig. 4 d) now compares the stress triaxiality profile as a function of the normalized distance to the crack tip for three different positions along the thickness: center plane, quarter thickness and surface. The stress triaxiality near the free surface is much lower, tending to a pure plane stress state. Fig. 4 e) shows the variation of the distance between the crack tip and the position X^{peak}, at which the maximum opening stress and stress triaxiality is attained. This distance is the same whether considering the opening stress or the stress triaxiality. Furthermore, with increasing J and post-crack initiation, this distance increases linearly, indicating that the maximum values for both quantities are reached further away from the crack tip as the crack propagates. Finally, Fig. 4 f) shows the variation of the equivalent plastic strain as a function of the normalized distance to the crack tip at an instant close to cracking initiation and then at several levels of J during crack growth, i.e. $J/\sigma_0 l_{nl} = 0.6, 2.8, 5.7, 6.9, 7.7, 8.5, 9.5, 10.4, 11.3, 12.3, 13.1$.

Fig. 5 illustrates the propagation of cracks and the degree of necking that develops ahead of the crack front, which amounts with the present materials parameters to about 20% thickness reduction. Note that more than 50% thickness reduction is not uncommon in tough ductile metallic plates (Pardoen et al., 2004). Fig. 5 a) shows that the crack propagates from the center towards the edges of the specimen leading to the so-called "crack tunneling" phenomenon. Once the crack reaches a length equal to half the specimen's thickness, as shown in Fig. 5 b), it approximately starts at the edges. Crack tunneling becomes more evident in Figs. 5 c) and d), i.e. when it has

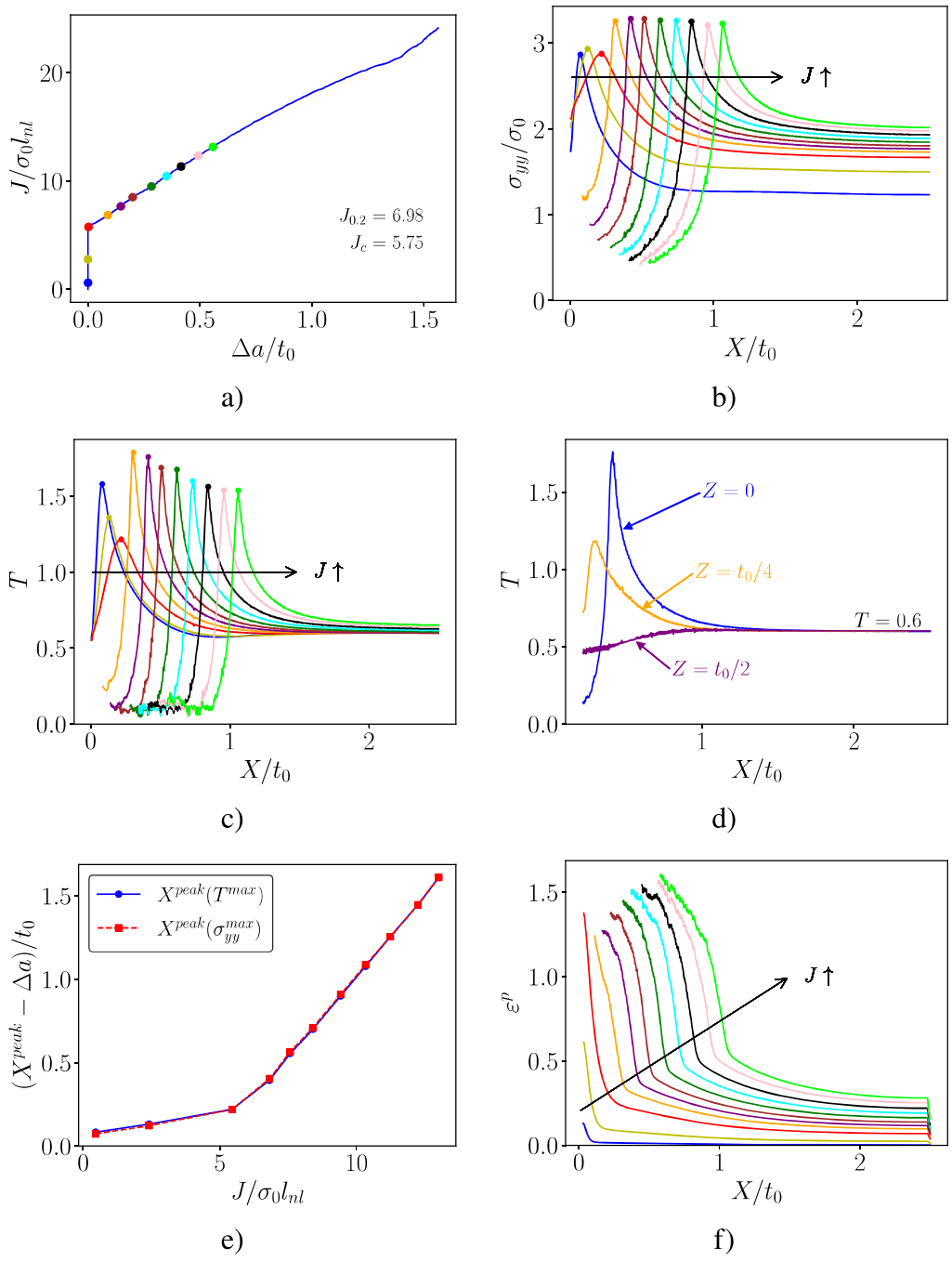

Figure 4: Simulation of crack growth in a DENT specimen characterized by $n = 0.1$, $f_0 = 10^{-2}$, $t_0 = 2$mm, $l_{nl} = 100\mu$m. a) J_R curve with markers indicating the value of J considered for plotting other relevant quantities; b) opening stress evolution as a function of the normalized distance to the crack tip for different values of J; c) stress triaxiality evolution as a function of the normalized position for different values of J; d) stress triaxiality at cracking initiation as a function of the normalized distance to the crack tip for three different positions along the thickness ; e) distance between the coordinate at which the peak of the opening stress/stress triaxiality is attained and the position of the crack tip; f) equivalent plastic strain evolution as a function of the normalized position for different values of J. X represents the position in the undeformed configuration.

propagated more than one specimen thickness. Tunneling comes from that the fracture strain is larger along the specimen edges due to the lower local stress triaxiality compared to the center plane. Furthermore, the degree of necking increases during crack propagation in agreement with several experimental findings (Pardoen et al., 1999). These are not the first full 3D FE simulations of ductile crack growth including a detailed analysis of the local stress fields and characteristics of the cracking process with a GTN model, but the number of similar simulations remains small in the literature especially in the context of a non-local numerical formulation.

Fig. 6 illustrates the evolution of the thickness reduction factor, denoted as $r_f = \frac{t_0 - t_f}{t_0}$, where t_0 is the initial thickness and t_f is the current thickness. In Fig. 6 a), the thickness reduction is shown along the ligament for various values of J. The degree of necking increases as the crack grows and reaches a stable value that depends on the loading conditions. After a certain extent of crack propagation, the necking ahead of the crack tip stabilizes at a value of 0.38, as depicted in Fig. 6 b), while the initiation value is about 0.19.

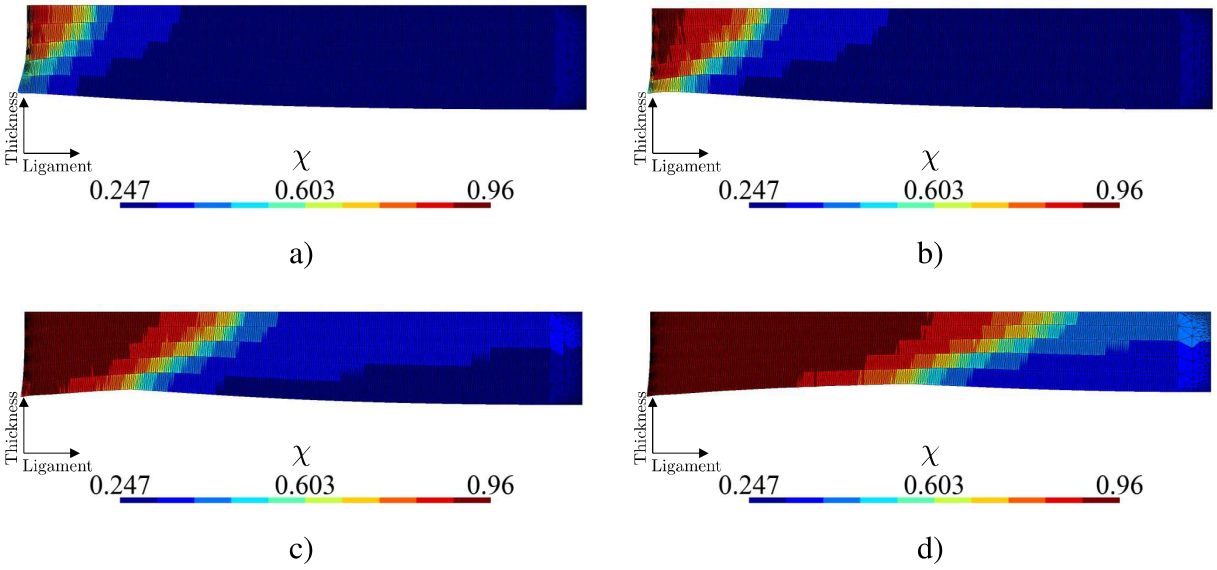

Figure 5: Crack propagation in the ligament plane at different loadings for a DENT specimen characterized by $n = 0.1$, $f_0 = 10^{-2}$, $t_0 = 2$mm, $l_{nl} = 100\mu$m. a) $\Delta a \approx 0.2t_0$; b) $\Delta a \approx 0.5t_0$; c) $\Delta a \approx 1t_0$; d) $\Delta a \approx 2t_0$.

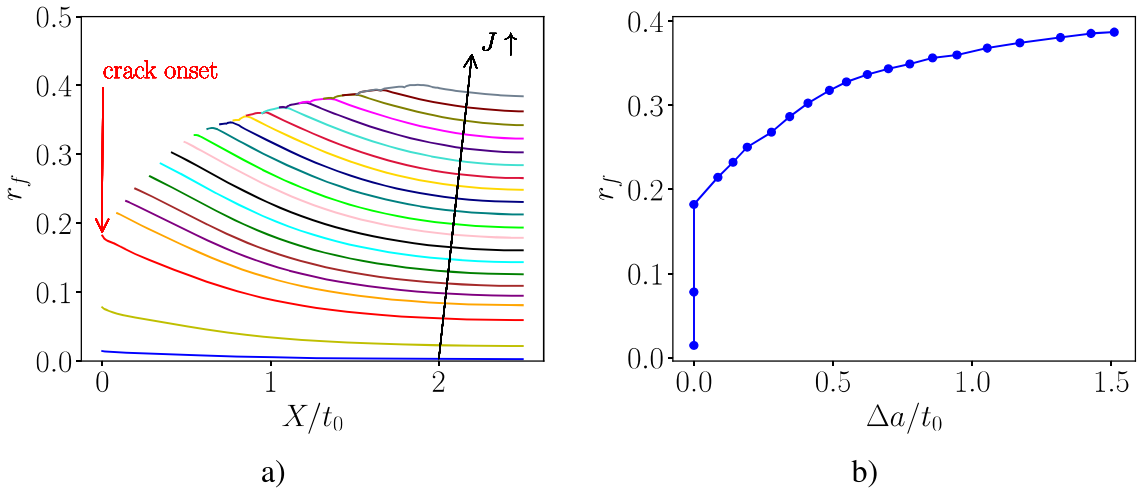

Figure 6: Reduction factor at different loadings for a DENT specimen characterized by $n = 0.1$, $f_0 = 10^{-2}$, $t_0 = 2$mm, $l_{nl} = 100\mu$m. a) r_f evolution as a function of the normalized position for different levels of J; b) r_f in front of the crack tip as a function of the normalized crack length.

4. Thickness effect in ductile crack growth

The literature has repetitively reported that the thickness of cracked specimen has a significant effect on the ductile crack growth resistance, e.g. Anderson (2005); Broek (1982). For instance, Pardoen et al. (1999) have used DENT specimens of different thicknesses (1 to 6 mm) to study this effect. The tests were analyzed based on the J integral and on the essential work of fracture approach indicating a strong increase of the toughness with increasing thickness. Similar effects were observed in Shahani et al. (2010) on steel plates with thicknesses ranging from 1.25 to 4.06 mm, using CT specimens together with an anti-buckling system. An initial increase of the fracture toughness followed by a decrease above a critical thickness was found. Such a behavior was simulated using a local version of the GTN model in Rivalin et al. (2001) for anisotropic steel plates.

4.1. Simulation strategy

The effect of the dimensions of both CT and DENT specimens is studied here using the non-local Gurson model 2 of Table 1 with a focus on the effect of plate thickness. Two levels of initial porosity are considered: $f_0 = 0.01$ (high porosity/lower toughness) and $f_0 = 0.001$ (low porosity/higher toughness). The corresponding GTN parameters have been gathered in Table 2. Regarding the numerical procedures, the elements in which the failure criterion is reached for half of the Gauss points are automatically removed from the simulation. In regions where the stress triaxiality is particularly low such as next to the blunted crack tip close to the free surface, the elements become extremely elongated without breaking because the critical porosity is not attained. In this case, elements in which the local accumulated plastic strain is larger than 3 are also removed from the simulation. This could physically correspond to an instantaneous failure by secondary void nucleation corresponding to, *e.g.* the formation of shear lips or simply be an artifact to the

simple critical porosity criterion that does not work well in some circumstances. This condition is only activated in the simulations with a low porosity ($f_0 = 0.001$).

For each specimen geometry (CT and DENT), two series of simulations are performed: one with homothetic specimens of different sizes and one with specimens of different thicknesses while keeping all other dimensions constant. The specimens are referred to as CT_{WBB} (resp. DENT_{WBB}) where W is the width of the specimen and B its thickness. The standard CT specimens correspond to the case where $W = 2B$. In the case of homothetic CT and DENT specimens, the width is varied from $W = 6.25$ mm to $W = 100$ mm with $W = 2B$ and $a_0/W = 0.55$ as recommended in the ASTM E1820 standard. In the practice, specimens with W smaller than 10 mm are very difficult to machine and test. Specimens are sketched in Fig. 1. $\mathrm{CT}_{25\mathrm{B}12.5}$ and $\mathrm{DENT}_{25\mathrm{B}12.5}$ specimens are used as references when varying the thickness between 1 mm and 25 mm. In this last case, $B = W$, which corresponds to a very thick specimen. In all cases, side grooves are added to the specimens with a net thickness $B_N = 0.8B$. Linear hexahedral elements are used with full integration. The mesh is highly refined in the region of crack growth. The number of elements used to discretize the thickness of the specimens varies from 9 for $B = 1$ mm to 108 for $B = 50$ mm leading to very heavy simulations. The mesh is finely refined over a distance of 2.5 mm from the crack tip. The calculations are automatically stopped when the crack reaches the end of the refined zone. Results are analyzed in terms of J—Δa curves and $J_{0.5}$ values (corresponding to crack advance of 0.5 mm).

4.2. Results for CT specimens

Fig. 7 shows contour plots of the opening stress and damage fields in a $\mathrm{CT}_{25\mathrm{B}12.5}$ specimen for an average crack advance of $\Delta a = 1.99$ mm. Despite the side grooves, the crack front is not straight, showing some degrees of tunneling as discussed in Section 3. As expected, the stresses have dropped down to zero at locations where damage has reached the critical value at failure. Fig.

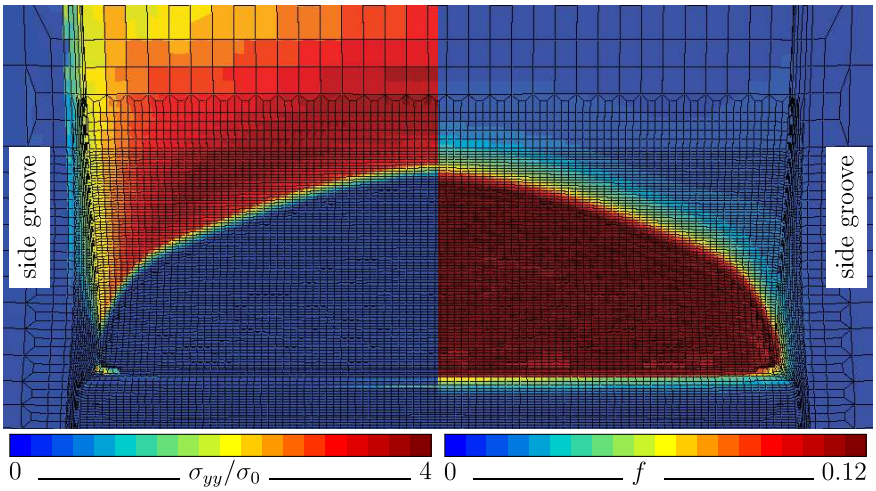

Figure 7: Opening stress (σ_{yy}/σ_0) and damage (f) in a $\mathrm{CT}_{25\mathrm{B}12.5}$ specimen for an average crack advance of $\Delta a = 1.99$ mm.

8 a) shows the J—Δa curves for homothetic CT specimens with $f_0 = 0.01$. The specimen size hardly affects the crack growth resistance. Fig. 8 b) shows similar curves for CT specimens with

different thicknesses while all other dimensions are kept the same. In this case, the thickness has an effect on the J—Δa curves. The exclusion lines for a crack advance of 0.2 mm and 0.5 mm are also shown on the graphs. Following the ASTM E1820 standard, the slope of these curves is equal to $2\sigma_Y$ where σ_Y is the average of the 0.2% offset yield stress and the ultimate tensile stress (equal to $\sigma_0(k_k n)^n \exp(-n + 1/k_k)$ using the proposed hardening law). $J_{0.2}$ and $J_{0.5}$ values correspond to the intersection of the J—Δa curves with the exclusion lines. In the following, $J_{0.5}$ values are used to compare the different specimens.

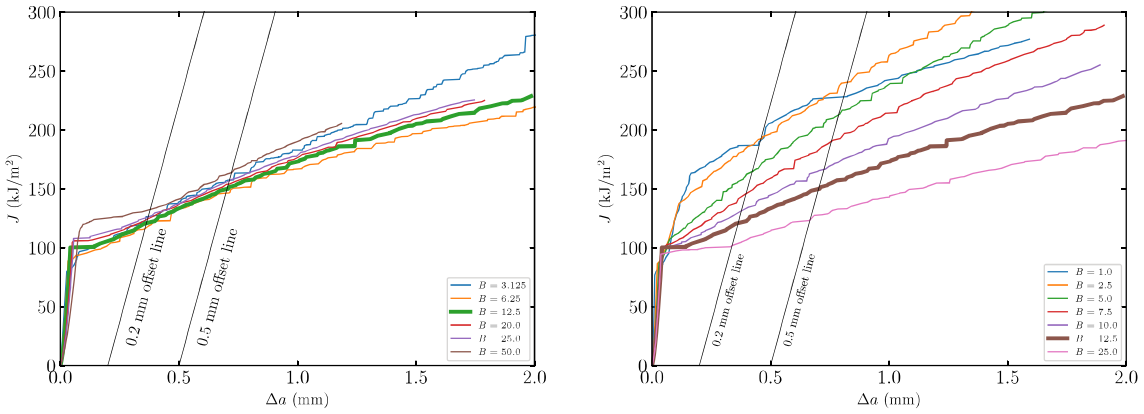

(a) (b)

Figure 8: (a) J—Δa curves for homothetic CT specimens. (b) J—Δa curves for variable thickness CT specimens. ($f_0 = 0.01$).

Fig. 9 shows the variations of the $J_{0.5}$ values as a function of the specimen thickness for the two sets of simulations. Fig 9 a) corresponds to the low toughness case ($f_0 = 0.01$). On the one hand, $J_{0.5}$ is almost constant for homothetic CT specimens even in the case of very small specimens (which, as noted above, are almost impossible to machine and test in the practice). On the other hand, in CT specimens with different thicknesses, $J_{0.5}$ initially increases with thickness and then decreases for $B > 2.5$. Fig. 9 b) corresponds to the case where $f_0 = 0.001$, showing a much stronger increase of the fracture toughness compared to $f_0 = 0.01$ and $f_0 = 0.001$. This last trend is the one described in classical fracture mechanics textbooks. However, for the homothetic CT specimens, an almost constant $J_{0.5}$ value is found, again, as for the $f_0 = 0.01$ case. For specimens with varying thicknesses, $J_{0.5}$ reaches the maximum value for $B \approx 5$ mm and then decreases. Comparing both porosity levels indicates that the critical value of the thickness for which $J_{0.5}$ reaches its maximum increases when the overall toughness of the material increases (hence with lower initial porosity). The thickness at the peak toughness is around 1.5 mm and 5 mm for the initial porosity $f_0 = 0.01$ and $f_0 = 0.001$, respectively. As indicated by the dimensional analysis, the results will depend on the ratio l_{nl}/t_0. Hence, this thickness at peak toughness will scale with l_{nl} (as well as with the other parameters of the model). Note that for $B = 1$ mm and $f_0 = 0.001$, failure is triggered by the local accumulated plastic strain reaching 3 at numerous Gauss points.

In order to further unravel the origin of the effect of thickness on the fracture toughness, the stress state is analyzed at the position $X = 10l_{nl} = 1$ mm ahead of the crack tip at the center of a CT specimen with $f_0 = 0.001$. Results for $f_0 = 0.01$ exhibit similar trends. The stress triaxiality

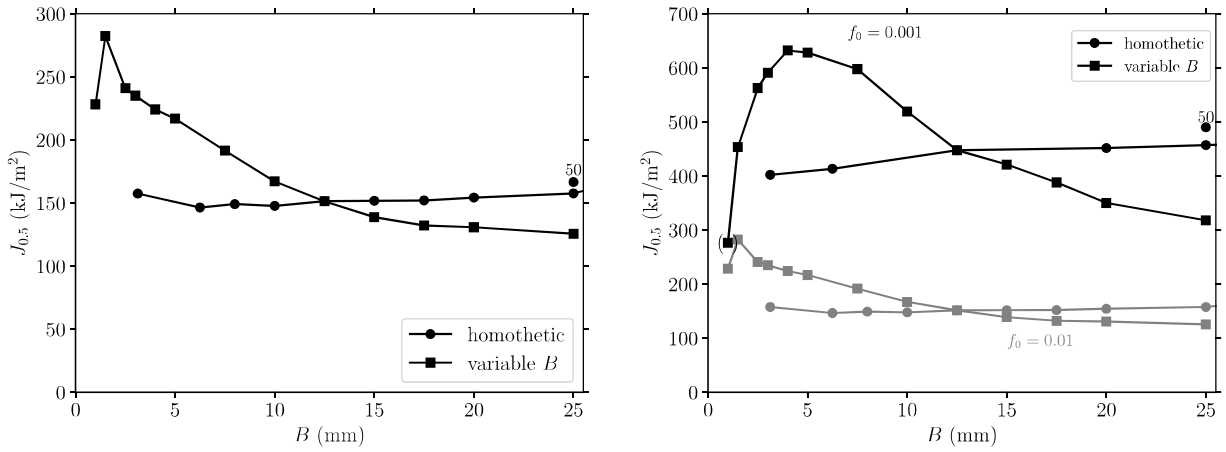

$f_0 = 0.01$ $f_0 = 0.001$

Figure 9: Simulated $J_{0.5}$ values for CT specimens

and Lode parameters are plotted as a function of the non-local accumulated plastic strain $\overline{\kappa}$ in Fig. 10. The Lode parameter is defined as:

$$\mathcal{L} = \frac{27}{2}\frac{\det(\boldsymbol{\sigma})}{\sigma_{\text{eq}}^3}, \tag{12}$$

where σ_{eq} is the von Mises stress and $\boldsymbol{\sigma}$ is the deviatoric stress tensor. $\mathcal{L}$ is defined so that $\mathcal{L} = 1$ for pure tension. $\mathcal{L} = 0$ for pure shear or plane strain. The role of the Lode parameter in ductile fracture has been studied by many authors Nahshon and Hutchinson (2008); Bai and Wierzbicki (2008); Papasidero et al. (2015) and it is well recognized that, at a given stress triaxiality, ductility is minimum for $\mathcal{L} = 0$. Analyzing this effect is out of the scope of this paper; however, examining the evolution of the Lode parameter provides insights into the loading history of the material in front of the crack tip.

Fig. 10 a) shows the variation of the stress triaxiality as a function of the nonlocal accumulated plastic strain for homothetic CT specimens with $f_0 = 0.001$. As expected, the largest maximum triaxiality (equal to 2.7) is reached for the thickest specimens and along the center plane. It decreases with thickness and reaches a minimum value of 2.15 for the smallest specimen ($B = 3.125$ mm). This drop is moderate and leads to non-local strains at failure between 0.28 and 0.36. These trends are consistent with the limited influence of the thickness on the $J_{0.5}$ values for homothetic CT specimens. The variations of the stress triaxiality for the CT specimens with various thicknesses but with the other dimensions kept constant are shown in Fig. 10 b). In this case, the maximum triaxiality is reached in the unusually thick specimen ($B = 25$ mm) with a value of 3.0. The key finding is that the decrease of the stress triaxiality with increasing thickness is much more pronounced than in the homothetic case. The minimum value is equal to 1.5 for $B = 1$ mm, along the center plane. The evolution of the stress triaxiality as a function of strain also strongly depends on the thickness. This results in fracture strains ranging from 0.28 to 0.75. Similar trends are found for $f_0 = 0.01$ (low toughness) but the stress triaxiality levels are higher, reaching 3.8 for the very thick specimens.

Fig. 10 c) and 10 d) show the variation of the Lode parameter as a function the nonlocal accumulated plastic strain for homothetic and varying CT specimen thicknesses, respectively. The evolution of $\mathcal{L}$ is complex for all specimens. In most cases, it starts with values close to -1, then rapidly reaches 1. As damage increases, $\mathcal{L}$ is close to 0.5. Interestingly, $\mathcal{L}$ always differs from 0 which corresponds to the plane strain case which is not reached even for the thickest specimens ($B = 25$ mm). This also contradicts the generally accepted idea that the center part of the specimens is under plane strain conditions.

The origin of the increasing fracture toughness with increasing thickness can now be explained in the following way based on the decomposition of the toughness J_c as the sum of a damage and fracture contribution Γ_0 and a necking contribution Γ_n : $J_c = \Gamma_0 + \Gamma_n$, see Pardoen et al. (2004). For very thin specimens and sufficiently low porosity, the local fracture strain attained in the fracture process zone is very large, leading to significant crack tip necking before cracking initiates. As the thickness increases, the degree of necking remains large and the work per unit area spent in crack tip necking Γ_n increases, simply because the volume of the neck increases as the cube of the thickness following the arguments and models developed in Pardoen et al. (2004) (Γ_n then increases almost proportional to thickness in the very small thickness regime). But, there is then a transition at which the stress triaxiality gets so large that the fracture strain decreases down to a level that does not allow anymore significant crack tip necking. The work of necking per unit area Γ_n progressively decreases to zero as the stress state progressively turns to plane strain. In the interval, there is a thickness at which the toughness is maximums.

Thickness effects occur when thickness is much smaller than the plane strain plastic zone size r_p which can be approximated by

$$r_p = \frac{1}{10}\frac{J_c}{\sigma_0}\frac{E}{\sigma_0}, \tag{13}$$

hence using Eq. (10),

$$r_p = \frac{1}{10}\frac{\sigma_0 l_{nl}}{\sigma_0}\frac{E}{\sigma_0}F = \frac{E}{\sigma_0}l_{nl}\frac{F}{10}, \tag{14}$$

because E/σ_0 in metals varies typically between 100 and 1000 and F between 3 and 300 (see also later in Section 6), thickness effects will start playing a role below a thickness (say about 3 times smaller than r_p) in the range 10 to 10000 l_{nl}. This is a very broad window. Knowing that l_{nl} varies physically between a few micrometers up to 100 micrometers as in this study, the effects can sometimes appear for plate thicknesses up to 10 cm or more which is beyond any experimental testing capabilities (and above most structural applications). It is then not a surprise that in the case of very tough stainless steels for instance, recent studies have shown that the plane strain plateau is not attained even with specimen thickness above 4.5 cm, Cheng et al. (2025). This discussion, although clearly showing the importance of this subject, remains however mainly qualitative and will be consolidated in future studies.

4.3. Results for DENT specimens

Similar simulations were performed for the DENT specimens. Examples of J—Δa curves are given in Fig. 11 a) for homothetic specimens. The value of $J_{0.5}$ is given here without considering

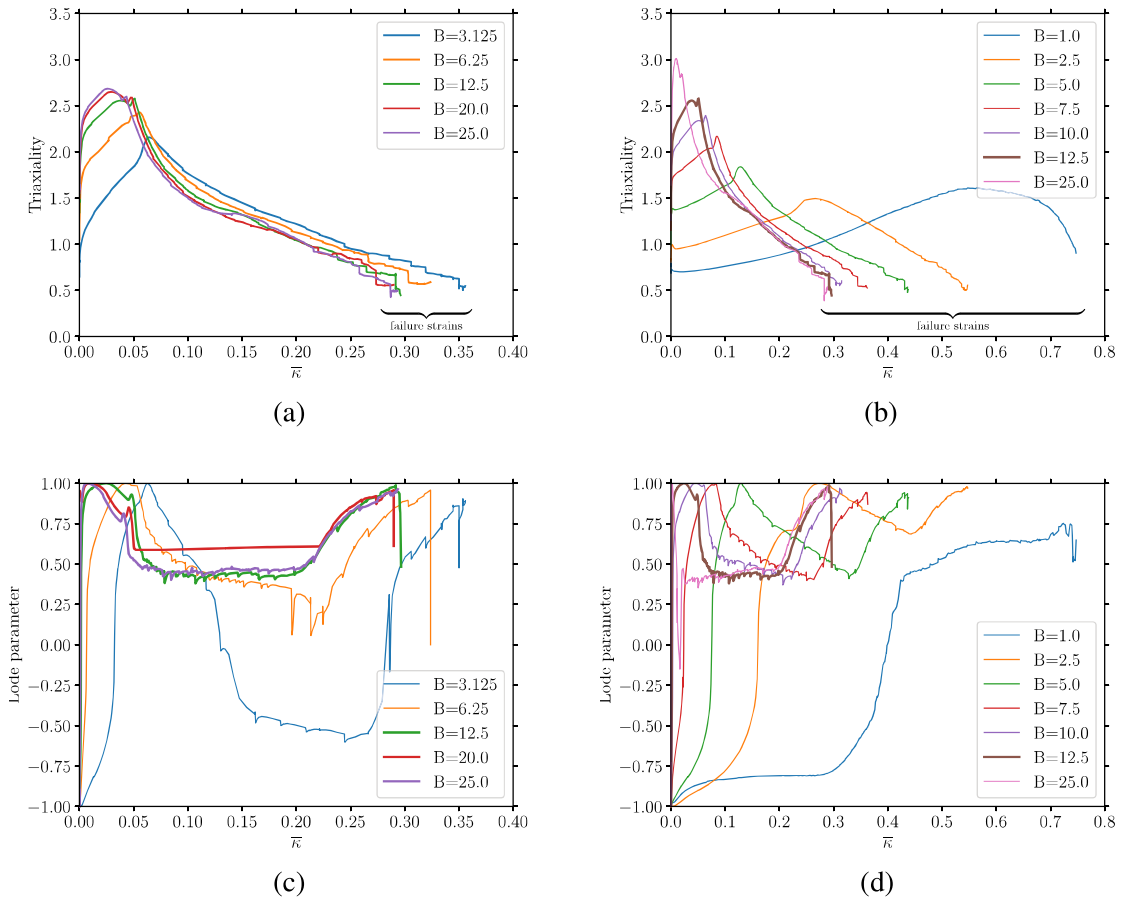

Figure 10: Variation of the stress triaxiality and Lode parameter as function of the non-local accumulated plastic strain $\overline{\kappa}$ at a position $X = 10l_{nl}$ along the center plane of CT specimens and $f_0 = 0.001$; stress triaxiality for (a) homothetic specimens, (b) similar specimens with different thicknesses; Lode parameter for (c) homothetic specimens, (d) similar specimens with different thicknesses

the exclusion line as its slope strongly differs from the computed blunting line. Fig. 11 b) shows the results in terms of $J_{0.5}$ as a function of specimen thickness for the two initial porosities and for the two families of specimens. The fracture toughness values are higher than those computed for CT specimens for both porosity levels. This is related to a geometry-based constraint effect which causes the stress triaxiality to be lower in specimens loaded in tension compared to specimens undergoing bending such as the CT specimen, see e.g. Thaulow et al. (2004).

The evolution of the stress triaxiality for both sets of specimens is shown in Fig. 12 for the low toughness case (maximum value of triaxiality is equal to 2.5). Evolutions for homothetic and varying thickness specimens are more similar compared to the CT specimens explaining why values of $J_{0.5}$ are similar for both cases. A similar trend is observed for the high toughness case with the maximum stress triaxiality further reduced to 2.1 (not shown). The stress triaxiality is, for thick specimens lower in DENT specimens compared to CT specimens, as mentioned above due to the lower constraint in tensile based test configurations. However, the decrease of the stress triaxiality with decreasing thickness is less marked than in CT specimens. This explains probably why the thickness effect appears smaller than in the CT specimens. A moderate increase is however observed for $f_0 = 0.001$. This indicates that the transition regime in DENT specimens before reaching the plane strain plateau is probably much wider with a peak toughness attained at much thicker specimens only. This aspect will be the focus of further studies as well.

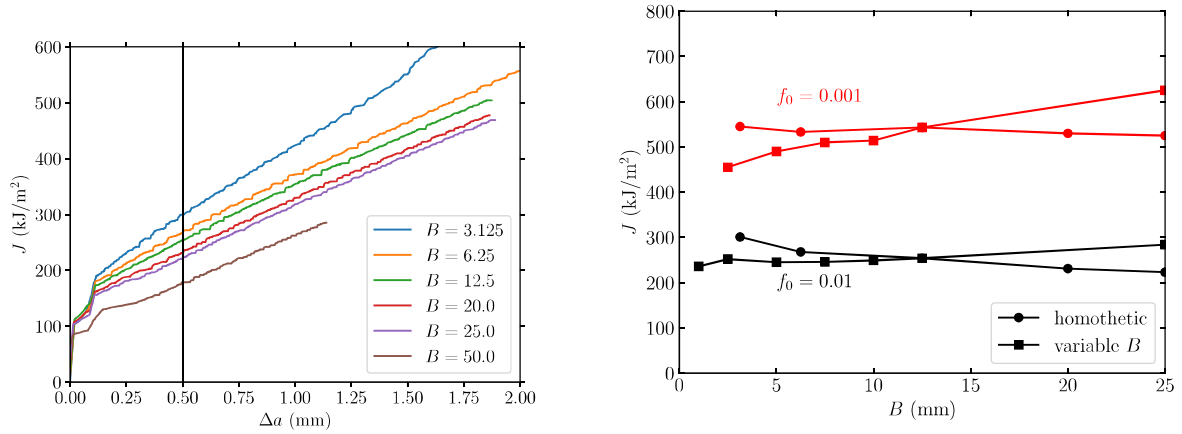

Figure 11: (a) DENT specimens ($f_0 = 0.01$) J—Δa curves for homothetic specimens. (b) Simulated $J_{0.5}$ values.

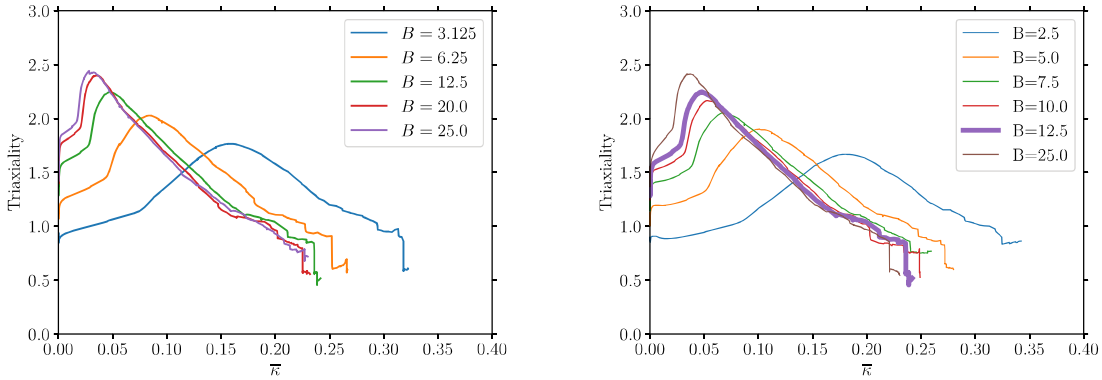

(a) Homothetic specimens (b) Varying specimen thickness

Figure 12: Variation of the stress triaxiality as function of the non-local accumulated plastic strain along the center plane of DENT specimens: (a) homothetic specimens. (b) similar specimens with Varying thicknesses. ($f_0 = 0.01$)

5. Effect of plastic anisotropy on ductile crack growth in thin sheets

The extension of the Gurson model to plastic anisotropy has been implemented in Code 1 in a general manner, as described in Nguyen and Pardoen (2025). In this study, only the elementary Hill model Hill (1948) has been considered but more complex yield functions are possible. The formulation is based on the driving stress expressed in the material configuration as:

$$\boldsymbol{\sigma}^{'} = \mathbf{R}^{a} \cdot \boldsymbol{\sigma}^{c} \cdot \mathbf{R}^{aT}, \tag{15}$$

where $\boldsymbol{\sigma}$ is the Cauchy stress, and $\mathbf{R}^{a}$ characterizes the rotation from the corotational configuration to the initial configuration. The Hill effective stress is given by:

$$\Sigma_e(\boldsymbol{\sigma}^{'}) = \sqrt{F(\sigma^{'}_{22} - \sigma^{'}_{33})^2 + G(\sigma^{'}_{33} - \sigma^{'}_{11})^2 + H(\sigma^{'}_{11} - \sigma^{'}_{22})^2 + 2L\sigma^{'2}_{23} + 2M\sigma^{'2}_{31} + 2N\sigma^{'2}_{12}}. \tag{16}$$

The coefficients F, G, H, L, M, and N are six material constants defining the degree of plastic anisotropy. When $F = G = H = 1/2$ and $L = M = N = 3/2$, the von Mises plastic yield surface is recovered. Eq. (16) can be rewritten in tensor notation as

$$\Sigma_e = \sqrt{\frac{3}{2}\boldsymbol{\sigma}^{'} : \mathbf{M} : \boldsymbol{\sigma}^{'}}, \tag{17}$$

where $\mathbf{M}$ is the fourth-order tensor that characterizes plastic anisotropy.

The hydrostatic stress is defined as

$$\Sigma_h = \frac{\text{trace}(\boldsymbol{\sigma}^{'})}{3} = \frac{\text{trace}(\boldsymbol{\sigma}^{c})}{3}, \tag{18}$$

and, as defined in Eq. (A.15), directly enters the GTN yield locus as expressed in Appendix A. In this study, simple transverse isotropy is assumed, characterized by a single Lankford coefficient

r_L. This implies an in plane isotropic plastic behavior but a different strength in the thickness direction z, further assumed to be constant throughout the deformation process. The yield stress in the thickness direction relates to the in-plane yield stress σ_0 as:

$$\sigma_{0z} = \sigma_0 \sqrt{\frac{1 + r_L}{2}}. \tag{19}$$

3D FE simulations are performed for three Lankford coefficients r_L equal to 0.5, 1 (isotropic case) and 2 for a DENT panel with the following dimensions $t_0 = 2$ mm, $2L_0 = 20$ mm, $2W_0 = 60$ mm, $2H_0 = 150$ mm. Simulations are conducted by using the q_1, q_2, κ, α and β parameters identified for each r_L values for $n = 0.1$, $n = 0.3$ and $f_0 = 0.01$ with $k = 666$, using 3D void cell simulations relying on the Hill model instead of J_2 plasticity, as explained in Appendix B. The values are gathered in Table 4. Some calculations are also run with the values q_1, q_2, κ, α and β parameters identified for $r_L = 1$, in order to check whether the fine-tuning of these fitting parameters as a function of r_L has a major impact or not on the predictions.

Table 4: GTN-Thomason parameters for isotropic and anisotropic cases

Isotropic Case ($r_L = 1$)					
n	q_1	q_2	κ	α	β
0.1	1.080	0.920	0.549	0.919	1.995
0.3	1.987	0.714	1.206	0.030	1.758
$r_L = 0.5$					
0.1	1.090	0.941	0.513	1.570	1.878
0.3	1.845	0.741	0.705	0.063	1.726
$r_L = 2$					
0.1	1.520	0.817	0.727	1.0569	1.890
0.3	1.532	0.770	0.806	0.323	1.962

Fig. 13 gathers the results obtained for $f_0 = 0.01$ and $n = 0.1$ for the different r_L and the different choices made for adjusting the parameters q_1, q_2, κ, α and β. Fig. 13 a) compares the force displacement curves. As expected, plastic anisotropy has a significant effect on the maximum load that is attained, increasing with increasing r_L. Fig. 13 b) shows the J_R curves. The resistance to crack growth is enhanced for increasing r_L. There are only very few studies to which these results can be compared and critically discussed. The work of Tvergaard and Legarth (2004) is one of these. However, it uses a cohesive zone model to represent the failure process, which does not capture the impact of the plasticity anisotropy on the fracture process zone response - plastic anisotropy "only" affects the plastic dissipation in the continuum around the FPZ. Qualitatively, the magnitude of the effect of anisotropy is similar to here. The difficulty for making comparison to experimental data is that most of the time plastic anisotropy is convoluted with the morphological anisotropy associated to the voids. The morphological anisotropy, as vastly studied for instance by

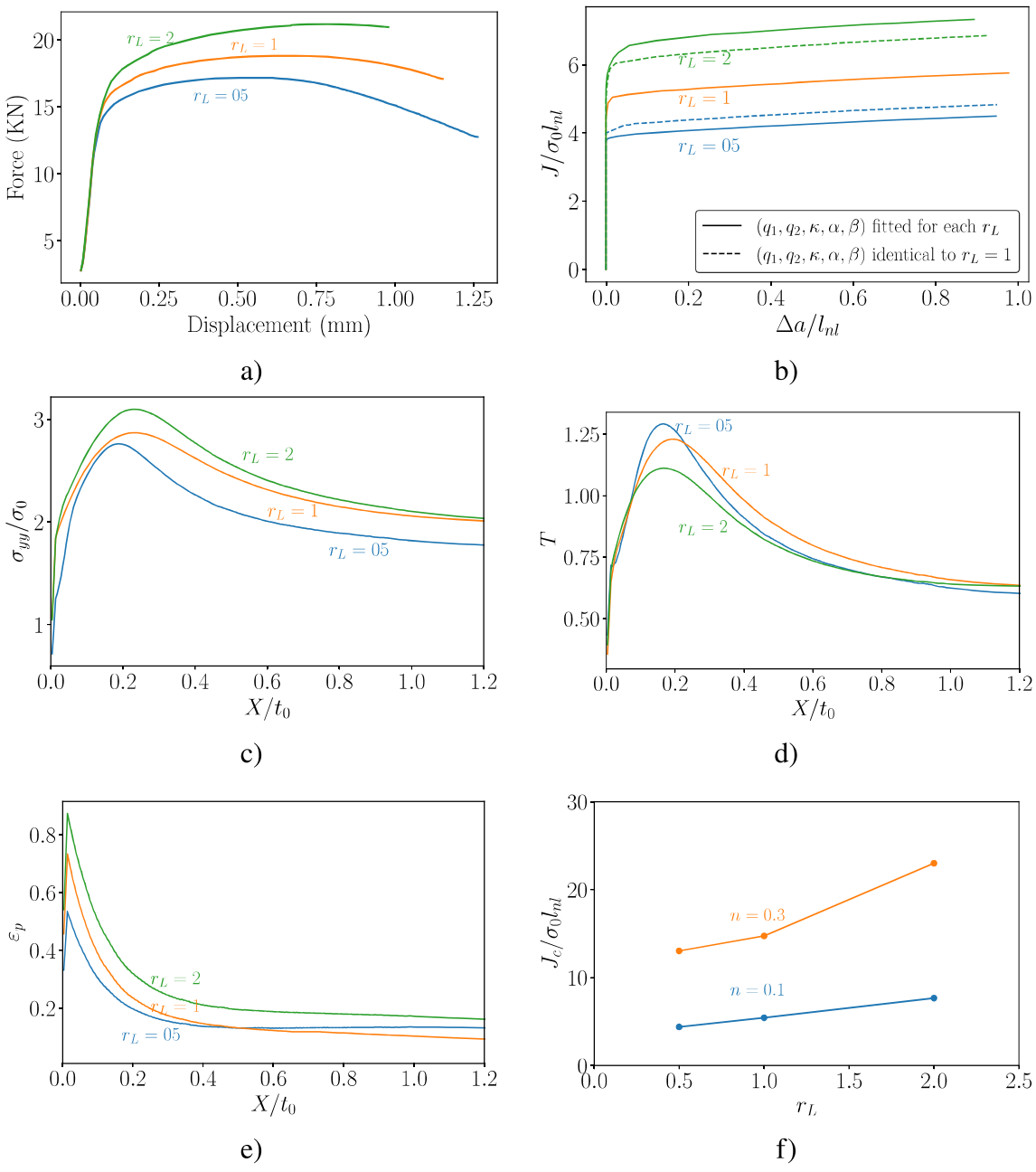

Figure 13: Simulation of crack growth for a material characterized by $f_0 = 0.01$ and $n = 0.1$ for the different r_L: a) force-displacement curves; b) J_R curves; c) opening stress variation as a function of the normalized position; d) stress triaxiality variation as a function of the normalized position; e) accumulated plastic strain as a function of the normalized position; f) fracture toughness as a function of the Lankford coefficient for different values of the strain hardening.

Benzerga and Besson (2001), Shinohara et al. (2016) or also by Pardoen and Hutchinson (2003), is associated to the second phase particles that are often preferentially aligned and elongated in the rolling or extrusion directions. This leads to both heterogenous distribution (that can be captured by λ_0 different than 1) and marked void shape effect (with usually prolate voids nucleating when loading is applied along the rolling direction). The morphological anisotropy leads to significant effects that will thus add to the plastic anisotropy on crack growth. Note that the main trends are captured without fine-tuning q_1, q_2, κ, α and β as a function of r_L but the impact of using the adjusted values is not negligible.

Figs. 13 c), d) and e) show the variations of the maximum principal stress, stress triaxiality and equivalent plastic strain respectively, as a function of the distance to the crack tip. The stresses are larger for large r_L as expected. However, a higher r_L leads to lower stress triaxiality and larger equivalent plastic strain. This shows that the conditions inside the fracture process zone vary with r_L in a complex way. Hence, a larger r_L leads to larger stresses and strains, hence, larger dissipation in the fracture process zone explaining the enhancement of the fracture toughness. Fig. 13 f) presents the variation of the fracture toughness J_c normalized by the yield stress σ_0 and internal length l_{nl} as a function of r_L for different values of n and $f_0 = 0.01$. the plastic anisotropy effect is amplified at high strain hardening exponent.

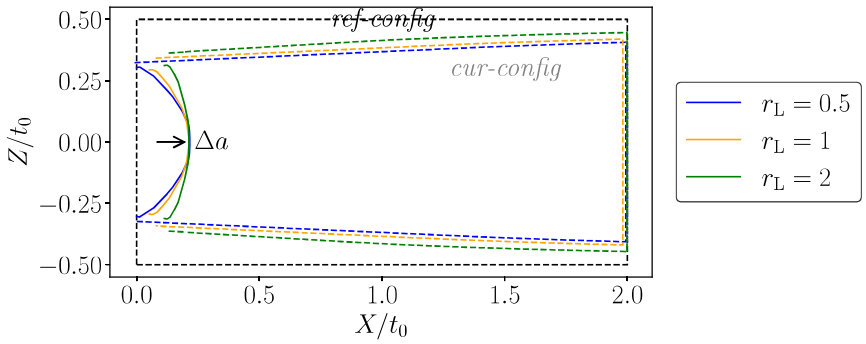

Figure 14: Necking profile for a material characterized by $f_0 = 0.01$ and $n = 0.1$ for the different Lankford coefficients.

Fig. 14 illustrates the impact of the plastic anisotropy on the degree of necking by showing the reduction of section on the fracture surface. A small r_L leads to a larger reduction of thickness. This indicates that if J_c is again decomposed into the two contributions $\Gamma_0 + \Gamma_n$, a larger degree of necking (expressed by the thickness reduction at the crack tip) does not necessarily translate into a larger Γ_n. Indeed, Γ_n also depends on the magnitude of the stresses developing inside the necking region as well as on the elevation of the neck, see Pardoen et al. (2004).

6. Strain hardening effect on 3D ductile crack growth

Fig. 15 illustrates the impact of strain hardening on the ductile crack growth resistance, considering two thicknesses of DENT panels: $t_0 = 1$mm and $t_0 = 5$mm. In Figs.15 a) and b), an initial value of $f_0 = 10^{-2}$ is used, while in Figs.15 c) and d), f_0 is set to 10^{-3}.

Figs. 15 a) and c) indicate that crack initiation takes place before the peak of the force-displacement curve. Meanwhile, Figs.15 b) and d) show that both the fracture toughness and the tearing resistance significantly increase with higher values of n.

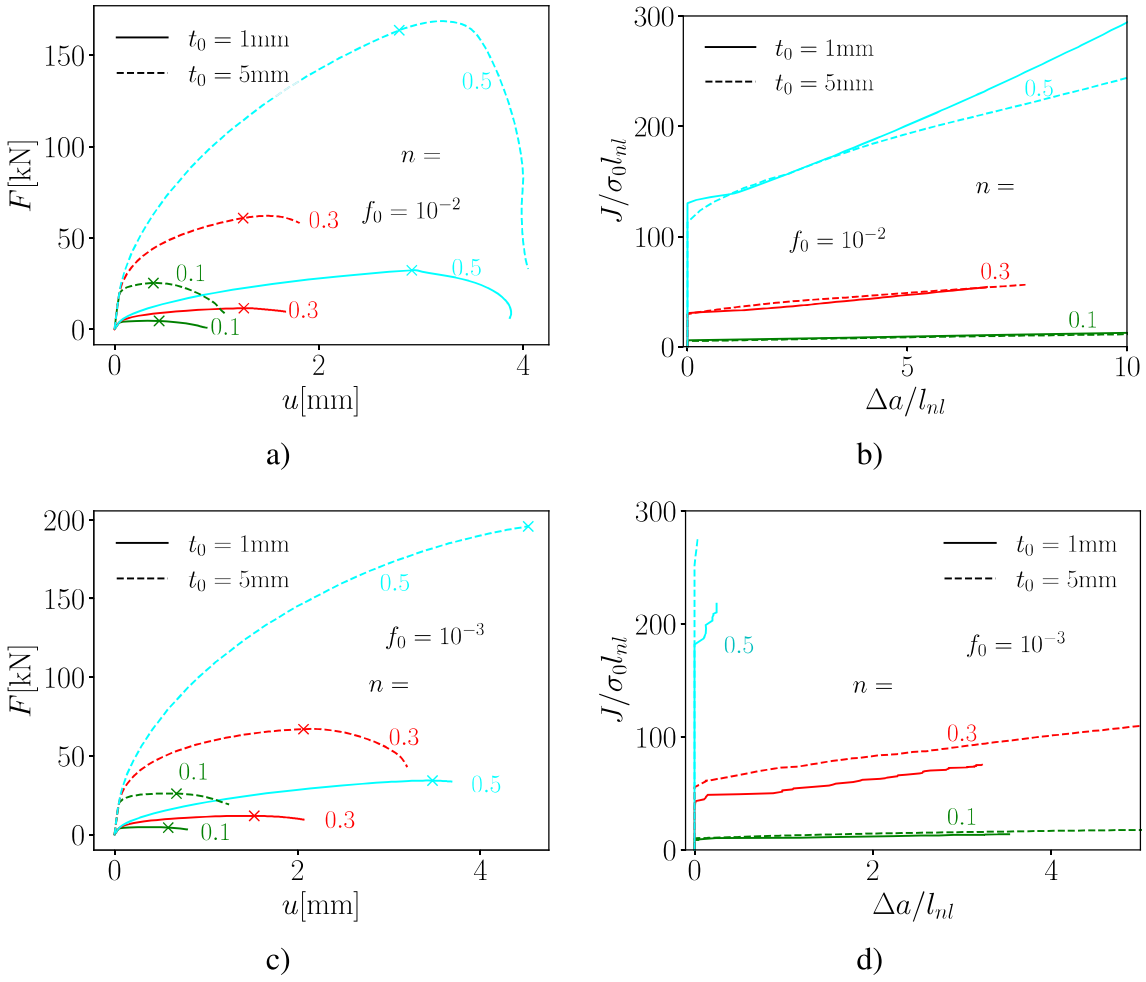

Figure 15: Strain hardening effect on the crack growth resistance of a material characterized by two different initial porosities f_0 for two different thicknesses of a DENT panel: a) force-displacement responses for $f_0 = 10^{-2}$; b) J_R curves for $f_0 = 10^{-2}$; c) force-displacement responses for $f_0 = 10^{-3}$; d) J_R curves for $f_0 = 10^{-3}$.

Fig. 16 a) illustrates the relationship between the fracture toughness and strain hardening for two different initial porosity values. The increase of the fracture toughness (FT) is more pronounced when $n \geq 0.3$ for both values of f_0, in line with the detailed analysis described in Kaniadakis et al. (2025) limited to 2D plane strain conditions. This effect appears even more important in thin metal plates. The initial thickness does not impact much the magnitude of the fracture toughness for $f_0 = 10^{-2}$. However, for $f_0 = 10^{-3}$, in line with the results of Section 4, the thickness has a significant effect; specifically, a larger thickness corresponds to a higher fracture toughness. Fig. 16 b) depicts the reduction factor measured at the initial crack tip as $r_f = (t_0 - t_f)/t_0$, with t_f the current thickness. The reduction factor r_f increases almost linearly with strain hardening n

for both initial porosity and thickness values. This signifies more dissipation at the crack tip with increasing n. In Pardoen et al. (2004) and further elaborated by Hilhorst et al. (2023), the height of the neck also increases with increasing n, leading to more energy spent in necking Γ_n. Fig. 16 c) illustrates the normalized critical crack tip opening displacement as a function of strain hardening. As previously noted in Kaniadakis et al. (2025), the influence of the strain hardening exponent n is less significant here compared to its effect on fracture toughness. For both values of initial porosity f_0 and both initial thicknesses, there is a nearly linear increase in fracture toughness (FT) with increasing n. Additionally, Fig. 16 d) depicts the morphology of the initial crack tip at the point of crack onset for $f_0 = 10^{-3}$ and varying values of strain hardening. For $n = 0.1$, the crack tip aligns almost parallel to the ligament direction. However, as n increases, the extent of blunting becomes more pronounced, particularly for $t_0 = 5$ mm.

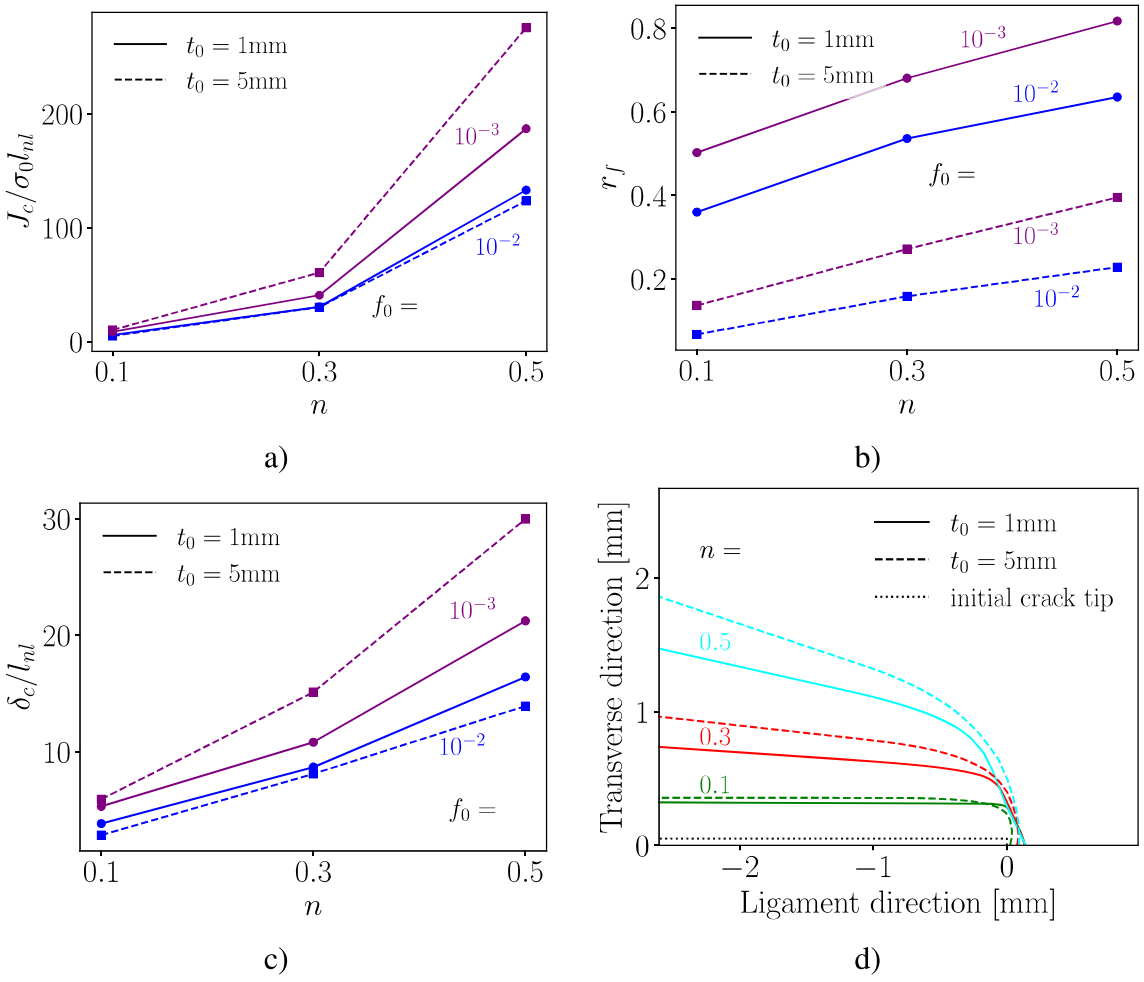

Figure 16: Strain hardening effect on the resistance to crack growth of a material characterized by two different initial porosities f_0 and two different thicknesses of a DENT panel: a) variation of the fracture toughness as a function of n; b) variation of the relative thickness reduction factor as a function of n; c) variation of the critical crack tip opening displacement as a function of n; d) shape of the current crack tip for $f_0 = 10^{-3}$.

A more in-depth description of the necking process is provided in Fig. 17. Fig. 17 portrays

the morphology of the crack area and of the necking region for different loading levels that give the same crack advance Δa. For t_0 = 1mm, Fig. 17 shows a) that increasing n involves a larger thickness reduction close to the initial crack tip, but also a more elevated neck in the loading direction (not shown). The morphology of the crack is also influenced by n since increasing n implies a less curved crack front. For t_0 = 5mm, Fig. 17 b) also shows more thickness reduction close to the initial crack tip. For the three values of n, the crack front is not flat but curved. The degree of tunneling is more significant for n = 0.1, and is reduced for n = 0.3 and n = 0.5. The necking process in front of the crack is also affected by n, with a thickness reduction increasing with n.

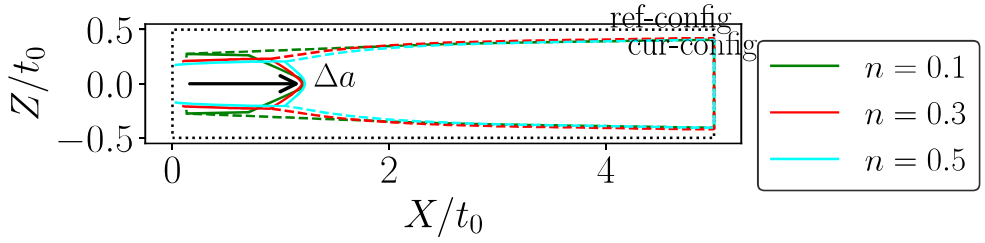

a)

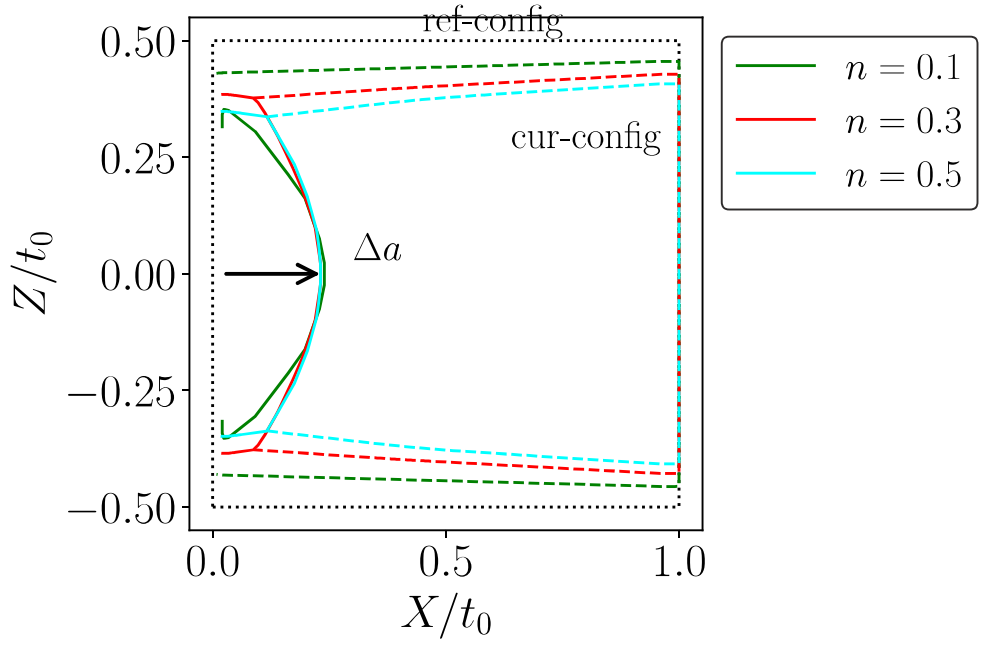

b)

Figure 17: Effect of strain hardening on the morphology of the crack front and on necking for two different thicknesses of the DENT panel at a loading leading to the same amount of crack growth along the center plane: a) t_0 = 1mm; b) t_0 = 5mm.

7. Conclusions and perspectives

The field of micromechanics of ductile fracture has reached today a high level of maturity. The state of art constitutive models for porous plasticity rely on a rich description of the physical mechanisms of damage by the nucleation, growth and coalescence of voids. The progress in high resolution in-situ x-ray microtomography combined to a wide range of test geometries and configurations provide large database of experimental results for the identification and validation, from local void by void information to overall failure conditions under varying stress states. And, the numerical treatment of these constitutive models, mainly via the finite element method, is quite robust. Here, we demonstrate that it is indeed possible today to perform 3D finite strain simulations allowing for long ductile crack growth under different loading configurations and this within a non-local framework and an advanced micromechanical description. These simulations reveal important information about the effect of the material and geometrical parameters on the resistance to ductile crack growth, which are still not well properly understood or captured by more empirical approaches. This includes:

- *The effect of plate thickness on the fracture toughness and tearing resistance*. We have shown that the available models do capture the variation of the fracture toughness first increasing with thickness and then decreasing down to the plane strain regime. The quantitative understanding of this phenomenon, commented for decades in classical fracture mechanics textbook (e.g. Broek (1982)), remains up to now elusive. The results described in this paper indicate that the degree of crack tip necking, the distribution of plastic strain and the stress triaxiality convolute to set the amplitude of this effect. But, more work is under progress to nail down the effect of all relevant parameters on the magnitude of the thickness effect in order to guide materials engineers towards making higher toughness metal plates and to guide structural designers to better take this effect into account when performing integrity assessment analysis. Among others, the amplitude of the thickness effect appears more modest in this study than what is sometimes found in very ductile metallic alloys, see e.g. Pardoen et al. (2004). Remember that this thickness effect takes place within a range of thickness between 0.1 and 100 mm (and even more) with a lot of practical consequences. This is at least true for specimens with the same profile and varying thicknesses but otherwise similar geometry.

- *The effect of specimen dimensions*. Aside from the thickness effect "alone", different fracture toughness was predicted, at the same thickness, depending on the other specimen dimensions and test configurations. In the case of homothetic CT specimens (with all dimensions modified and not only the thickness), the thickness effect disappears. This is related to the distribution of plastic strain in the near crack tip region influenced by the overall specimen dimensions. This marked constraint effect raises even more questions on the true meaning and validity of traditional fracture mechanics indicators such as J_c or δ_c for very tough metals when dealing with 3D effects. In particular, it questions the transferability of data generated on laboratory specimens to real structures when dealing with tough alloys even when testing at the same thickness. This gives much credits to pursuing in parallel the development of micromechanics-based simulation methods, but also on extending the use of other overall

parameters such as the essential work of fracture, e.g. Cotterell et al. (2005), Pardoen et al. (2004).

- *Plastic anisotropy effects on ductile crack growth.* Although the effect of plastic anisotropy on ductile crack growth was expected (Benzerga and Besson (2001), Nguyen and Pardoen (2025)), the results shown in this paper indicate that the effect gets particularly important when dealing with thin plates. Indeed, the energy associated to the crack tip necking process will very much depend on the degree of plastic anisotropy, here captured by a single Lankford coefficient, that will favor or restrain the development of the neck and the energy spent per unit area in crack tip necking. The preliminary analysis addressed in this work, based on a simple Hill type anisotropic yield locus, obviously requires more systematic and advanced investigations.

- *Strain hardening effects on ductile crack growth.* A new generation of metallic alloys has been designed during the last decade with significant strain hardening capacity, similar also to stainless steels or traditional bronze and brass. Here, we insist on that increasing the strain hardening capacity has a very significant impact on the fracture toughness. This is true in 2D plane strain conditions, as analyzed in more details elsewhere in the case of ideal small scale yielding conditions (Kaniadakis et al., 2025), but we demonstrate here that it is even more important in 3D cases. Indeed, in 3D, the energy dissipation associated to crack tip necking is very much influenced by strain hardening, as already anticipated in the literature with closed form models, see Pardoen et al. (2004), Hilhorst et al. (2023).

Now, even though the formalism used in this study is already quite advanced, it remains relatively academic compared to a large number of real ductile crack growth problems in industrial materials and real components. Except for the fact that voids are assumed to be immediately present in the material with no delayed void nucleation, one can consider that the predictions made in this study correspond to ideally ductile and tough materials, providing a sort of upper bound on the resistance to crack growth of ductile metals. Indeed, real metallic alloys and ductile failure problems potentially involve

- *voids of different sizes* which always tend to globally increase the void growth rate, e.g. Tvergaard (1998), due to interaction effects.

- *heterogenous void distribution* with some small or significant degree of clustering. In general, coalescence takes place with nearest neighbors inside more clustered regions. The calculations here somehow assume a periodic distribution. This effect can be heuristically taken into account through playing with a void distribution parameter λ_0 larger than 1, but more rigorous approaches should be elaborated.

- *second or third populations of voids* can nucleate early or late in the damage process, leading to an increase of the porosity not accounted for in this study. Such extra populations of voids are known to play a major role on accelerating the void coalescence process, e.g. Fabrègue and Pardoen (2008), with significant reduction of the fracture strain and favours the slant fracture mode.

- *local stress concentrations* always exist in materials due to microstructure features such as grain boundary, grain orientation and second phases, e.g. Lecarme et al. (2014). Voids located in these regions will grow and coalesce faster leading to lower local fracture strains. In particular, in dual phase alloys, the soft matrix regions between hard second phases undergo significant elevation of the stress triaxiality, hence faster void growth.

- *determination of the material parameters* from experimental data still remains a challenge, and no generic methodology has been proposed nor accepted by the users' community while the GTN is now widely used. This task is particularly difficult in cases which, as in this study, involve crack propagation. In addition, the internal length(s) should also be determined. Maybe, the internal length could be tuned on very small samples for which a size effect related to the material length should exist.

All these effects tend to accelerate the damage process, explaining why the local fracture strain in real fracture process zones can be lower than expected with the ideal models sometimes by one order of magnitude. This will directly lead to an abatement of the fracture toughness and of the crack growth resistance compared to the predictions given in this study. Most of these effects can be taken into account in the current framework in a reasonably physical way at the cost of introducing one or more extra materials parameters. Note that void shape effects can play a significant role on the void growth and coalescence process (Madou and Leblond (2012a,b), Morin et al. (2016), Scheyvaerts et al. (2010)). Void shape effects are crudely taken into account here through the fitting of the q_1 and q_2 parameters for the void growth phase. Furthermore, the present study has not addressed the complicated issues related to the transition from flat mode I to mixed mode I/III slant fracture (see e.g. El-Naaman and Nielsen (2013), Morgeneyer and Besson (2011), Besson et al. (2013)), which can for instance limit the thickness effect addressed in Section 4 of this paper, to plastic localization (as connected to the previous problem, see Kong et al. (2022)) and to mixed mode I/II crack growth problems. Our view is that all the phenomena and effects listed above can be important, with potentially first order effects, which constitute the short-term roadmap for the field and which can rely on relatively simple modification/evolution of the present framework. However, one should be careful at complexifying much more the present models. Ingredients should be introduced probably only one by one and not all together to avoid making the model and simulation untractable in terms of number of parameters to identify and computational intensity.

Finally, a major field of progress that paves the way for the next decades of research is the treatment of failure modes competing with the ductile mode:

- *Ductile-cleavage transition in ferritic steels.* Studies essentially under 2D plane strain conditions were performed already two or three decades ago combining a description of the ductile fracture process with a GTN based approach and a descriptor of cleavage based on the Beremin model (Ruggieri and Dodds (2018), Xia and Shih (1996), Samal et al. (2008), Tanguy et al. (2006)). Such analysis should be reassessed today in the context of a 3D non-local framework. This is particularly important in the context of a long term operation of the current fleet of fission nuclear reactors beyond 60 years, for which the irradiation dose will keep accumulating, increasing the importance of looking at the transition to cleavage. Note that strain gradient plasticity effects can play a major role on the void growth rate if

voids are submicron size, which is not so common in typical metallic alloys. Strain gradient plasticity can also affect the stress distribution in the near crack tip region when the crack tip opening remains sufficiently small, which happens when dealing with cleavage fracture in steels. Note that none of these last two effects are taken into account with the present non-local formulation whose role is "only" to introduce a length scale (noted l_{nl} here) associated to the void spacing.

- *Ductile-transcrystalline brittle*. Aside from the ductile-brittle transition in ferritic steels motivated very much by nuclear applications, the transition from ductile to brittle is particularly important in the context of hydrogen embrittlement. At low H_2 partial pressure, the mechanism of failure is fully ductile but then, with increasing H_2 charging, transition from ductile to mixed ductile/brittle and then to purely brittle is observed, see Lopes Pinto et al. (2024), Lin et al. (2022), Yu et al. (2016). A GTN type model is certainly meaningful in the first fully ductile regime but not in the purely brittle regime. The transition regime with brittle facets in between dimples could potentially be treated with a modification of the failure/coalescence model based on a critical stress-based criterion in the intervoid ligament and/or a modified void nucleation criterion, see Depraetere et al. (2023). In any case, it is very interesting to envision, on the long run, a framework that would encompass all the regimes from purely ductile to purely brittle in this context of H_2 effects.

- *Ductile versus intergranular brittle*. Another transition, sometimes found in high strength steels is the emergence of intergranular failure, as a function of the stress state. High strength steels, subjected to high stress triaxiality, can indeed involve extremely high local stresses on the grain or phase boundaries and induce their decohesion with low dissipation. Intergranular brittle fracture can also be favoured by corrosion effects, liquid metal embrittlement, diffusion of embrittling species like phosphorus in steels under irradiation or other mechanisms (Pineau et al., 2016). The combination of such chemical embrittlement effects inside a ductile fracture framework like the present model to produce failure maps is an interesting and practical field of further investigation

- *Ductile versus intergranular ductile*. In a number of metallic alloys, a competition exists between trans- and intergranular ductile crack growth, often related to the presence of softer precipitate free zones next to grain boundaries. The intergranular mode, although ductile as treated in this paper with the nucleation, growth and coalescence of cavities, usually leads to low fracture toughness. Attempts have already been made to model such phenomena with advanced Gurson models, e.g. Pardoen et al. (2010), but further work needs to be done to predict the transition regimes.

- *Ductile versus creep*. The mechanisms of failure during creep also involve the nucleation, growth and coalescence of voids, essentially along grain boundaries, but driven by diffusion of vacancies and viscoplasticity associated to dislocation climb (Van Der Giessen et al. (1997), Onck and van der Giessen (1998), Gaffard et al. (2005)). There is a rich playground to develop models that can naturally transition from low-moderate temperature failure (as

properly captured with models such as the one proposed here, augmented with viscoplasticity) and higher temperature creep dominated failure.

- *Ductile versus low cycle fatigue*. The mechanisms of ductile failure under low cycle fatigue are similar to the monotonic phenomenon except that the process is modified by the cyclic nature of the plasticity problem. This includes the first order impact of kinematic hardening effects, see Leblond et al. (1995). Although progress keeps being made in this direction (Besson (2009), Roubaud et al. (2024)), there is still room for developing models that encompass monotonic and low cycle fatigue under various loading configurations.

All these exploration lines constitute a roadmap for a field that has been revitalized very much in recent years. Indeed, metallic alloys are considered again at the front of the scene owing to novel progress on the metallurgy side with TRIP/TWIP alloys, very clean metallurgical processes, HEA, and additive manufacturing, but also because of their recyclability and durability. If properly manufactured and used, these materials fail by ductile fracture which remains thus ubiquitous for proper failure assessment and life extension of a number of human technologies.

Acknowledgements

This work has received funding from the European Research Council (ERC) under the European Union's Horizon 2020 research and innovation programme (Grant agreement No. 101097433). Computational resources have been provided by the supercomputing facilities of the Consortium des Équipements de Calcul Intensif en Fédération Wallonie Bruxelles (CÉCI) funded by the Fond de la Recherche Scientifique de Belgique (FRS-FNRS).

Appendix A Non-local Gurson model

The non-local Gurson model/code 1 introduced by Nguyen et al. (2020) relies on two features summarized here below. The reader is referred to this last reference for more details.

On the one hand, the free-energy is defined by considering regular plasticity for the matrix material, *i.e.* without strain-gradient effects, and by adding to the elastic free energy ψ^e the functional

$$\sum_k h_k \left[\frac{\left(Z_k - \bar{Z}_k\right)^2}{2} + \frac{\nabla_0 \bar{Z}_k \cdot \mathbf{C}_k \cdot \nabla_0 \bar{Z}_k}{2} \right], \tag{A.1}$$

where $k = 1, ..., N$ represents the non-local mechanisms, a selection of local variables are represented by $\mathbf{Z}$ and their non-local counterparts by $\bar{\mathbf{Z}}$, $\mathbf{C}_k = l_k^2 \mathbf{I}$ denote the second order non-local length tensor, with l_k the non-local length associated with the non-local mechanism k, and h_k is an arbitrary coupling modulus. Besides, the local generalized internal mechanical power is defined in a fashion close to the micromorphic framework suggested by Forest (2009), by adding to the stress power the contribution

$$\sum_k h_k \left[\bar{\sigma}_k \dot{\bar{Z}}_k + \bar{M}_k \cdot \nabla_0 \dot{\bar{Z}}_k \right], \tag{A.2}$$

where $\bar{\sigma}_k$ and $\bar{M}_k$ are the conjugate thermodynamic forces to $\bar{Z}_k$ and $\nabla_0 \bar{Z}_k$, respectively. Applying the variational framework leads to a classical definition of the stress tensor from the elastic free energy ψ^e, and, to the following extra governing equations

$$\bar{Z}_k - Z_k - \nabla_0 \cdot \left(\mathbf{C}_k \cdot \nabla_0 \bar{Z}_k \right) = 0 \,. \tag{A.3}$$

Eventually, for small enough values of h_k, the contribution (A.2) does not affect the dissipation inequality.

As a result, the definition of the stress tensor and the relationship between the local and non-local variables (A.3) correspond to the implicit non-local model pioneered by Peerlings et al. (1998).

On the other hand, the extended version of the Gurson model/code 1 by Nguyen et al. (2020) presents three distinct mechanisms for describing ductile damage: void growth, internal necking void coalescence, and shear-driven void coalescence. This presentation will focus solely on the version of the model with void coalescence by internal necking, and so shear-driven coalescence will not be addressed.

To describe the distribution of voids, a representative cylindrical unit cell is used, featuring a void at its center. The dimensionless variables that characterize this unit cell include the porosity (f), the void aspect ratio (W), the void spacing ratio (χ), void distribution ratio (λ), and the main axis of the void ($\mathbf{e}_z$). The parameter γ defines the shape of the void, which may change during coalescence. For a spheroidal void, $\gamma = \frac{1}{2}$, whereas for a conical void, $\gamma = 1$. The relationship between these parameters are expressed as follows:

$$f = \frac{\chi^3 W}{3\gamma\lambda}. \tag{A.4}$$

The set of parameters $\mathbf{Y}$ describing the void characteristics reads

$$\mathbf{Y} = \begin{bmatrix} f & \chi & W & \lambda & \gamma & \mathbf{e}_z \end{bmatrix}^T, \tag{A.5}$$

with

$$\mathbf{Y}_0 = \begin{bmatrix} f_0 & \chi_0 & W_0 & \lambda_0 & \gamma_0 & \mathbf{E}_z \end{bmatrix}^T, \tag{A.6}$$

the vector with the initial values. The following equations characterize the porous plasticity model:

$$\Phi_{nl} = \Phi_{nl} \left(\boldsymbol{\sigma}; \sigma_Y, \mathbf{Y} \right), \tag{A.7}$$

$$\mathbf{D}^p = \dot{\mu} \mathbf{N}^p \left(\boldsymbol{\sigma}; \sigma_Y, \mathbf{Y} \right), \tag{A.8}$$

$$\boldsymbol{\sigma} : \mathbf{D}^p = (1 - f)\, \sigma_Y \dot{\varepsilon}_m, \tag{A.9}$$

$$\dot{\mathbf{Y}} = \dot{\mathbf{Y}} \left(\mathbf{Y}, \bar{\mathbf{Z}}, \boldsymbol{\sigma} \right), \tag{A.10}$$

$$\dot{\mu} \geq 0, \Phi_{nl} \leq 0, \dot{\mu} \Phi_{nl} = 0, \tag{A.11}$$

where Φ_{nl} is the yield function, σ_Y is the mean yield stress of the matrix computed with Eq.(1), $\mathbf{D}^p$ is the plastic strain rate, with plastic normal $\mathbf{N}^p$, μ is the plastic multiplier, and $\bar{\mathbf{Z}}$ is a vector representing all non-local variables. The deviatoric and volumetric equivalent plastic strain rates read

$$\dot{\varepsilon}_d = \sqrt{\frac{2}{3}\mathrm{dev}\left(\mathbf{D}^p\right) : \mathrm{dev}\left(\mathbf{D}^p\right)}, \qquad \dot{\varepsilon}_v = \mathrm{tr}\left(\mathbf{D}^p\right). \tag{A.12}$$

The matrix, deviatoric, and volumetric equivalent plastic strains are selected as local variables and represented by $\mathbf{Z}$, while their non-local counterparts are denoted as $\bar{\mathbf{Z}}$.

$$\mathbf{Z} = \begin{bmatrix} \varepsilon_v & \varepsilon_m & \varepsilon_d \end{bmatrix}^T, \qquad \bar{\mathbf{Z}} = \begin{bmatrix} \bar{\varepsilon}_v & \bar{\varepsilon}_m & \bar{\varepsilon}_d \end{bmatrix}^T. \tag{A.13}$$

Void growth phase: GTN model. Void growth is taken into account using the porous plasticity Gurson-Tvergaard-Needleman model (Needleman, 1980; Tvergaard, 1990). Eq. (A.7) particularized for the GTN yield function reads:

$$\Phi_{nl} = \Phi_G = \frac{\hat{\sigma}_G}{\sigma_Y} - 1, \tag{A.14}$$

with $\hat{\sigma}_G$ denoting the GTN effective stress

$$\hat{\sigma}_G\left(\sigma_{eq}, p', \sigma_Y, f\right) = \frac{\sqrt{\sigma_{eq}^2 + 2\sigma_Y^2 f q_1 \left[\cosh\left(\frac{3}{2} q_2 \frac{p'}{\sigma_Y}\right) - 1\right]}}{1 - q_1 f}. \tag{A.15}$$

where $\sigma_{eq} = \sqrt{\frac{3}{2}\mathrm{dev}(\boldsymbol{\sigma}) : \mathrm{dev}(\boldsymbol{\sigma})}$ is the equivalent von Mises stress, $p' = \frac{\mathrm{tr}(\boldsymbol{\sigma})}{3}$ is the hydrostatic stress, and q_1 and q_2 are the GTN fitting constants (the extension to plastic anisotropy is more recent and is presented in Section 5). The plastic normal to the GTN yield surface is

$$\mathbf{N}^p = \mathbf{N}_G^p = \sigma_Y \frac{\partial \Phi_G}{\partial \boldsymbol{\sigma}} = \frac{\partial \hat{\sigma}_G}{\partial \boldsymbol{\sigma}}. \tag{A.16}$$

Concerning the evolution laws of the void characteristics, according to Gurson's hypotheses, voids are initially spherical, meaning that $W_0 = 1$ and $\gamma_0 = 0.5$. The shape of the void during the growth phase remains spherical, hence $\dot{W} = 0$ and $\dot{\gamma} = 0$. The evolution laws of the variables $\mathbf{Y}$ are expressed as follows:

$$\begin{cases} \dot{f} = (1 - f)\dot{\bar{\varepsilon}}_v + A_n(\bar{\varepsilon}_m)\dot{\bar{\varepsilon}}_m \\ \dot{W} = 0 \\ \dot{\lambda} = \kappa\lambda\dot{\bar{\varepsilon}}_d \end{cases}, \tag{A.17}$$

with the void growth term $(1 - f)\dot{\bar{\varepsilon}}_v$ and the nucleation term $A_n(\varepsilon_m)\dot{\bar{\varepsilon}}_m$ (Chu and Needleman, 1980). A_n is the nucleation intensity function, κ represents the void spacing factor.

During void growth, the ligament χ follows

$$\chi = \left(\frac{3 f \lambda}{2}\right)^{\frac{1}{3}}. \tag{A.18}$$

Internal-necking void coalescence: MPS-based Thomason yield function. Eq.(A.7) with the Thomason yield function becomes

$$\Phi_{nl} = \Phi_T = \frac{\hat{\sigma}_T}{\sigma_Y} - 1, \tag{A.19}$$

where Φ_T indicates the Thomason yield surface, $\hat{\sigma}_T$ the associated effective stress

$$\hat{\sigma}_T = \frac{1}{C_{Tf}} \left(\frac{2}{3} \sigma_{eq} \cos\theta + |p'| \right). \tag{A.20}$$

In Eq.(A.20), C_{Tf} is the plastic constraint factor introduced in Pardoen and Hutchinson (2003), given by

$$C_{Tf} = \left(1 - \chi^2\right) \left[\alpha \left(\frac{1-\chi}{\chi W} \right)^2 + \beta \sqrt{\frac{1}{\chi}} \right], \tag{A.21}$$

where α and β are constants that depend on the strain hardening exponent (Pardoen and Hutchinson, 2000), and θ is the Lode angle given by $\theta(\sigma_{eq}, J_3) = \frac{1}{3}\arccos\frac{27 J_3}{2\sigma_{eq}^3}$, with $J_3 = \det(\mathrm{dev}(\boldsymbol{\sigma}))$. The plastic normal of Eq.(A.8) now becomes

$$\mathbf{N}^p = \mathbf{N}^p_T = \sigma_Y \frac{\partial \Phi_T}{\partial \boldsymbol{\sigma}} = \frac{\partial \hat{\sigma}_T}{\partial \boldsymbol{\sigma}}, \tag{A.22}$$

The evolution laws of the void characteristics are given by

$$\begin{cases} \dot{\chi} = \dfrac{3}{4}\dfrac{\lambda}{W}\left(\dfrac{3}{2\chi^2} - 1\right)\dot{\bar{\varepsilon}}_d \\ \dot{W} = \dfrac{9}{4}\dfrac{\lambda}{\chi}\left(1 - \dfrac{1}{2\chi^2}\right)\dot{\bar{\varepsilon}}_d \\ \dot{\lambda} = \kappa\lambda\dot{\bar{\varepsilon}}_d \end{cases}. \tag{A.23}$$

Effective yield surface. The competition among the two modes of porosity evolution: i.e. diffuse void growth introduced in Eq.(A.14) and internal necking coalescence (Eq.(A.19)), is modeled by defining an effective yield function, denoted as Φ_e

$$\Phi_{nl} = \Phi_e = \max\left(\Phi_G, \Phi_T\right). \tag{A.24}$$

Consequently, the space of admissible solutions is defined by the two yield surfaces, Φ_G and Φ_T. Eq. (A.24) can be rewritten as

$$\Phi_e = \frac{\hat{\sigma}}{\sigma_Y} - 1, \tag{A.25}$$

with

$$\hat{\sigma} = \max\left(\hat{\sigma}_G, \hat{\sigma}_T\right). \tag{A.26}$$

The onset of void coalescence is detected by

$$\dot{\varepsilon}_m > 0 \qquad \text{and} \qquad \hat{\sigma}_T > \hat{\sigma}_G. \tag{A.27}$$

This model was validated by comparing it to experimental data on high entropy alloys as reported by Hilhorst et al. (2022), accounting also for shear coalescence that is introduced through a third yield surface Φ_s and not presented in this appendix.

Appendix B Unit cell simulations and optimization procedure to find the GTN-Thomason parameters

Micromechanical analysis is performed on a unit void cell to actually quantify the effect of the stress state on the void growth and coalescence mechanisms similarly to the pioneering work of Koplik and Needleman (1988), followed by Besson (2009), Pardoen and Hutchinson (2000) and many others. The overall responses obtained from unit cell simulations are considered as the reference solutions from which the GTN/Thomason parameters of the model of Nguyen et al. (2020) including q_1, q_2, and κ, α, and β, can be identified.

B.1 Axisymmetric unit cell calculations under constant stress triaxiality

The unit cell consists of a spherical cavity located at its center, see Fig. B1. Since the material is assumed to be isotropic, the height and the diameter of the cylinder are equal, corresponding to an initial void aspect ratio $\lambda_0 = 1$. The initial porosity f_0 and the initial void ligament ratio χ_0 are respectively determined as:

$$f_0 = \frac{2}{3}\left(\frac{2R_0}{L_0}\right)^3 \qquad \chi_0 = \frac{2R_0}{L_0} = \left(\frac{3f_0}{2}\right)^{1/3}. \tag{B.1}$$

The material of the unit cell is represented by J_2 plasticity and isotropic elasticity.

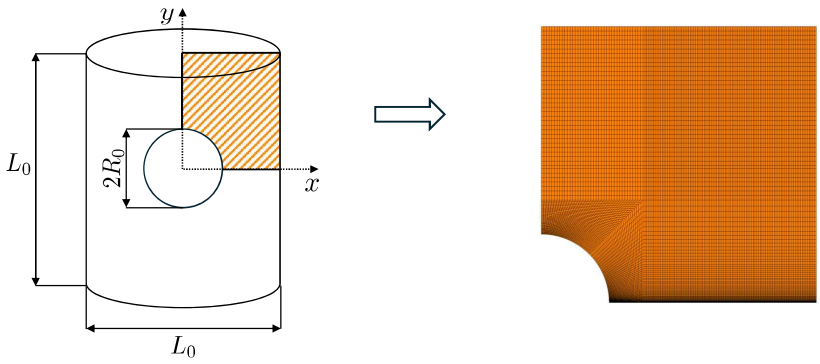

Figure B1: Axisymmetric cylindrical unit cell (left) and corresponding axisymmetric finite element mesh for $f_0 = 2 \cdot 10^{-3}$ (right).

Periodic boundary conditions imply that the unit cell edges remain straight. The unit cell simulations are performed for different values of f_0 and under different stress triaxiality. The finite element mesh consists of 9-node axisymmetric quadrilateral elements, see e.g. Fig. B1 right. The resulting macroscopic principal stresses along the axial direction Σ_{yy} and along the radial direction

Σ_{xx} are estimated by the average forces on the cell boundaries respectively following y and x per current area. The different stress measures are computed from:

$$p_{\text{cell}} = \frac{1}{3}(\Sigma_{yy} + 2\Sigma_{xx}), \tag{B.2}$$

$$\sigma_{VM} = |\Sigma_{yy} - \Sigma_{xx}|, \tag{B.3}$$

$$T_{\text{cell}} = \frac{p_{\text{cell}}}{\sigma_{VM}}, \tag{B.4}$$

where p_{cell} is the average pressure, σ_{VM} is the average von Mises equivalent stress, and T_{cell} is the average stress triaxiality, which is equal to the prescribed value. The current porosity is directly computed from the finite element mesh in the current configuration, such that:

$$f = \frac{V - \int_{V_0^s} J dV_0}{V}, \tag{B.5}$$

where V is the current cell volume whose initial value is $V_0 = \pi\lambda_0 L_0^3$, J is the determinant of the deformation gradient, representing local volume change of the solid part from the reference to the current configuration, V_0^s is the initial volume occupied by the solid part.

B.2 3D void cell calculations with plastic anisotropy

The 3D unit cell calculations follow the same approach as described in B.1. To account for plastic anisotropy, the unit cell matrix is modeled using the Hill anisotropic plasticity formulation, assuming transverse isotropy with the anisotropy axis aligned along the thickness direction (Z-axis) as shown in Fig. B2. Owing to symmetry, only one-eighth of the unit cell is simulated, with symmetric boundary conditions applied on the XY, XZ, and YZ planes. The overall deformation ratio between the in-plane (XY) and thickness (Z) directions is controlled by the Lankford coefficient r_L. For r_L=0.5, the unit cell deforms more in the thickness direction, leading to larger thinning, while for r_L=2 deformation is larger in the width (X) direction, reducing thickness thinning.

B.3 Optimization procedure

The overall response obtained from unit cell simulations are considered as the reference solutions to identify the values of q_1, q_2, κ, α, and β by assuming the plastic dissipation equivalence. On the one hand, under a given initial porosity f_0 and a given stress triaxiality T, a unit cell simulation allows deriving the following response:

$$\begin{bmatrix} \sigma_{VM}^{\text{UC}} \\ f^{\text{UC}} \end{bmatrix} = \mathcal{F}^{\text{UC}}\left(\bar{W}_m^{\text{pl,UC}}; T, f_0\right), \tag{B.6}$$

where σ_{VM}^{UC}, f^{UC} are respectively the homogenized von Mises stress and the current porosity, and $\bar{W}_m^{\text{pl,UC}}$ is the average plastic dissipation energy. The evolutions of f^{UC} and $\bar{W}_m^{\text{pl,UC}}$ are estimated by:

$$f^{\text{UC}}(t) = 1 - \frac{1}{V}\int_{V_0^{\text{solid}}} J dV_0, \tag{B.7}$$

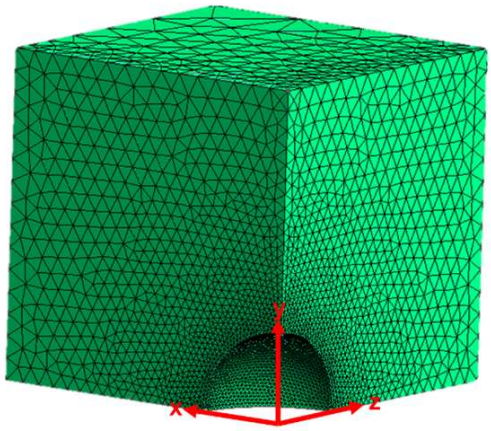

Figure B2: Axisymmetric cylindrical the unit cell and corresponding axisymmetric finite element mesh for the case of plastic anisotropy.

$$\bar{W}_m^{\mathrm{pl,UC}}(t) = \frac{1}{V_0}\int_0^t \left[\int_{V_0^{\mathrm{UC}}} J_m \boldsymbol{\sigma}_m : \mathbf{D}^p dV_0\right] dt, \tag{B.8}$$

where $V_0 = L_0^3$ is the initial volume, V is the current counterpart, and V_0^{solid} is the initial solid part. On the other hand, we consider the simulation of a homogeneous unit cube obeying the porous model with the initial porosity f_0. Under the constant triaxiality T, one has the following response:

$$\begin{bmatrix}\sigma_{VM}\\ f\end{bmatrix} = \mathcal{F}\left(\bar{W}^{\mathrm{pl}}; T, q_1, q_2, \kappa, g, h\right), \tag{B.9}$$

where σ_{VM} and f are respectively the von Mises stress and the current porosity, and $\bar{W}^{\mathrm{pl}}$ is the total plastic dissipation, which is estimated by:

$$\bar{W}^{\mathrm{pl}}(t) = \int_0^t \mathbf{P} : \left(\mathbf{F}^e \cdot \dot{\mathbf{F}}^p\right) dt = \int_0^t J\boldsymbol{\sigma} : \mathbf{D}^p dt. \tag{B.10}$$

Considering the best fit between the unit cell simulations (Besson, 2009) and the homogenized porous simulation (Kim et al., 2004) by the plastic dissipation equivalence, i.e., $\bar{W}_m^{\mathrm{pl,UC}}(t) = \bar{W}^{\mathrm{pl}}(t)\forall t$, one can define the following loss function to be minimized:

$$E(q_1, q_2, \kappa, g, h) = \sum_{i=1}^{4} \frac{1}{2}\left[\frac{\|f_i - f_i^{\mathrm{UC}}\|}{f_i^{\mathrm{UC}}} + \frac{\|\sigma_{VM,i} - \sigma_{VM,i}^{\mathrm{UC}}\|}{\sigma_{VM,i}^{\mathrm{UC}}}\right], \tag{B.11}$$

where the index i indicates the index of the i-th test with $T_i \in [1, 1.5, 2, 3]$, and the norm $\|\bullet\|$ is defined by:

$$\|\bullet\| = \int_0^{\bar{W}_{\mathrm{pl},m}^{\mathrm{last}}} |\bullet| d\bar{W}^{\mathrm{pl}}, \tag{B.12}$$

with $\bar{W}_{\mathrm{pl},m}^{\mathrm{last}}$ being the plastic dissipation at the end of the simulation. The parameters q_1, q_2, κ, α, and β are found by solving the following optimization problem:

$$(q_1, q_2, \kappa, \alpha, \beta) = \arg \min_{q_1,q_2,\kappa,\alpha,\beta} E(q_1, q_2, \kappa, \alpha, \beta), \tag{B.13}$$

subject to:

$$\begin{cases} 1 \leq q_1 \leq 3, \\ 0.2 \leq q_2 \leq 2, \\ 0.1 \leq \kappa \leq 1.5, \\ 0.01 \leq \alpha \leq 2, \\ 0.1 \leq \beta \leq 3. \end{cases} \tag{B.14}$$

A second option consists of following first

$$(q_1, q_2) = \arg \min_{q_1,q_2} E(q_1, q_2), \tag{B.15}$$

and then

$$(\kappa, \alpha, \beta) = \arg \min_{\kappa,\alpha,\beta} E(\kappa, \alpha, \beta), \tag{B.16}$$

with the same conditions of Eq.(B.14). This second method, although sometimes less "precise", is more physical. For both options, we consider the differential evolution, which is a gradient-free algorithm for global optimization, to solve the optimization problem of Eq.(B.14).

Appendix C Comparison of two models/codes

A preliminary comparison between the two codes, involving simple J_2 plasticity simulations, was conducted in Kaniadakis et al. (2025). This comparison demonstrated a perfect correspondence between the two codes. Now, moving on to the non-local GTN model used in this paper, the two codes are compared by performing the same simulation of a DENT panel with dimensions $2H_0 = 150$ mm, $2W_0 = 60$ mm, $2L_0 = 10$ mm, $t_0 = 2$ mm, and an initial crack tip opening $\delta_0 = 0.1$ mm, and using $f_0 = 0.01$ and $n = 0.1$.

Fig. C3 illustrates the comparison between the two models in terms of the force-displacement curve, the J_R curve, the stress triaxiality evolution as a function of the accumulated plastic strain at different distances X/l_{nl} from the initial crack tip (these are the two key parameters during the damage process), and the opening stress distribution corresponding to a loading level selected after the force-displacement peak. The agreement between the prediction of the two models is very good. The force-displacement curves in Fig. C3 a) of Code 1 and 2 align up to the crack initiation point (indicated with a cross), then they show some minor difference during crack propagation. As a matter of fact, the main difference between the two models is the treatment of the void coalescence process that can lead to differences in the energy dissipated and the evolution of stresses during the final stage of fracture of an element. As for the J_R curves, Fig. C3b) also demonstrates that Code 1 and 2 provide similar responses, with a difference below 10% in terms of the normalized fracture

toughness and comparable tearing moduli. Furthermore, Fig. C3 c) reveals a small difference regarding the maximum stress triaxiality attained at $X/l_{nl} = 1$ and the loading path. For other values of X/l_{nl} both models yield comparable results concerning the loading path. Fig. C3 d) illustrates a similar slope for the opening stress ahead of the crack, which initially follows the same trend, same peak, and then converges to the same value. This justifies the indistinct use of code to generate the results presented in the paper. As a matter of fact, Code 2 is used for Section 4 and Code 1 for Sections 5 and 6.

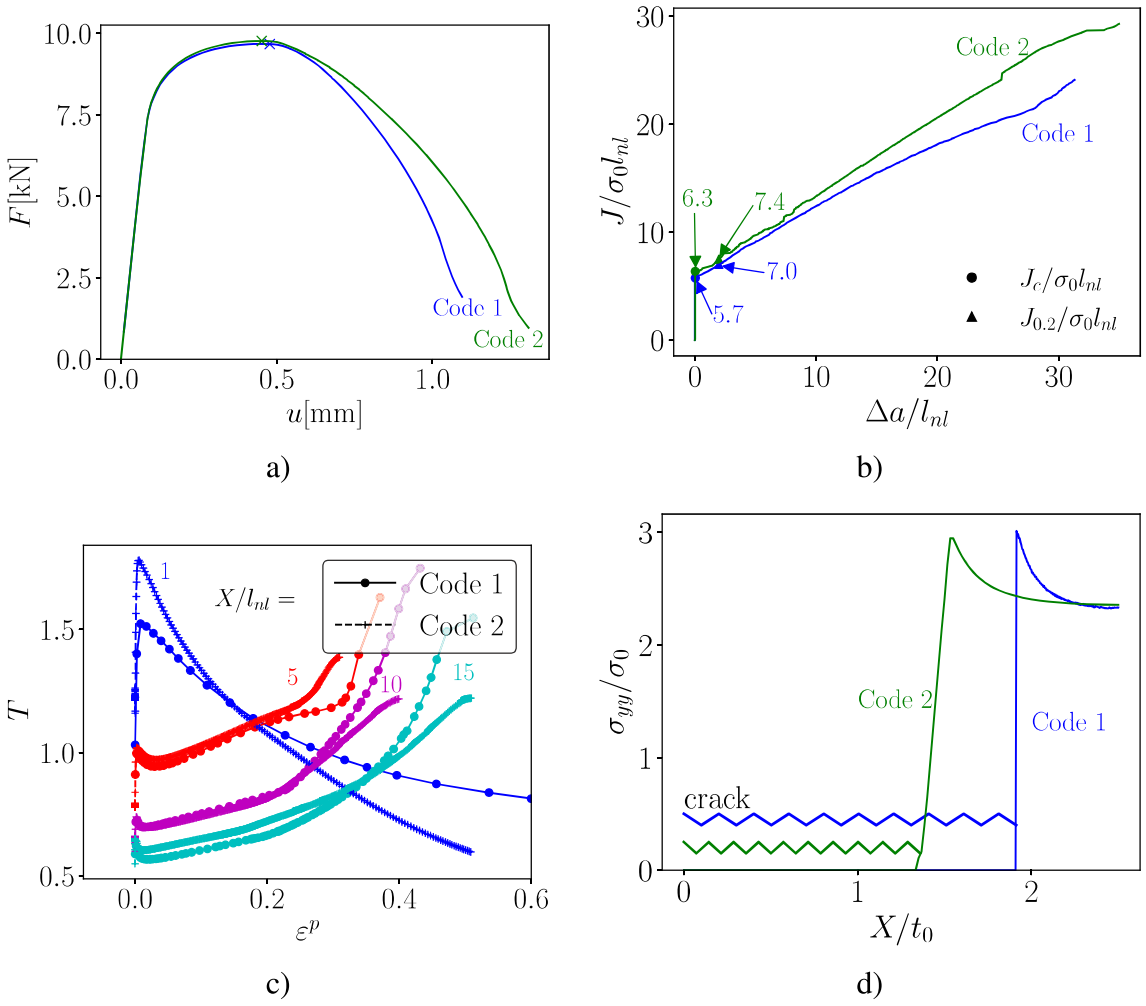

Figure C3: Comparison of the numerical results of the two models for a DENT specimen characterized by $n = 0.1$, $f_0 = 10^{-2}$, $t_0 = 2$mm, $l_{nl} = 100\mu$m. a) force-displacement curve; b) J_R curve; c) stress triaxiality evolution as a function the accumulated plastic strain at different distances from the initial crack tip; d) opening stress distribution on the center plane after the force-displacement peak at $F_{max}/2$.

References

Anderson, T.L., 2005. Fracture Mechanics: Fundamentals and Applications, Third Edition. CRC Press. URL: http://dx.doi.org/10.1201/9781420058215, doi:10.1201/9781420058215.

ASTM E1820, . Standard test method for measurement of fracture toughness. URL: http://dx.doi.org/10.1520/E1820-24, doi:10.1520/E1820-24. aSTM E1820-24.

Bai, Y., Wierzbicki, T., 2008. A new model of metal plasticity and fracture with pressure and lode dependence. International Journal of Plasticity 24, 1071–1096. URL: http://dx.doi.org/10.1016/j.ijplas.2007.09.004, doi:10.1016/j.ijplas.2007.09.004.

Bažant, Z.P., Jirásek, M., 2002. Nonlocal integral formulations of plasticity and damage: Survey of progress. Journal of Engineering Mechanics 128, 1119–1149. URL: http://dx.doi.org/10.1061/(ASCE)0733-9399(2002)128:11(1119), doi:10.1061/(asce)0733-9399(2002)128:11(1119).

Benzerga, A., 2002. Micromechanics of coalescence in ductile fracture. Journal of the Mechanics and Physics of Solids 50, 1331–1362. URL: http://dx.doi.org/10.1016/S0022-5096(01)00125-9, doi:10.1016/s0022-5096(01)00125-9.

Benzerga, A.A., Besson, J., 2001. Plastic potentials for anisotropic porous solids. European Journal of Mechanics - A/Solids 20, 397–434. URL: http://dx.doi.org/10.1016/S0997-7538(01)01147-0, doi:10.1016/s0997-7538(01)01147-0.

Benzerga, A.A., Leblond, J.B., 2010. Ductile fracture by void growth to coalescence, in: Aref, H., van der Giessen, E. (Eds.), Advances in Applied Mechanics. Elsevier. volume 44 of *Advances in Applied Mechanics*, pp. 169–305. URL: https://www.sciencedirect.com/science/article/pii/S006521561044003X, doi:https://doi.org/10.1016/S0065-2156(10)44003-X.

Besson, J., 2009. Damage of ductile materials deforming under multiple plastic or viscoplastic mechanisms. International Journal of Plasticity 25, 2204–2221. URL: http://dx.doi.org/10.1016/j.ijplas.2009.03.001, doi:10.1016/j.ijplas.2009.03.001.

Besson, J., McCowan, C., Drexler, E., 2013. Modeling flat to slant fracture transition using the computational cell methodology. Engineering Fracture Mechanics 104, 80–95. URL: http://dx.doi.org/10.1016/j.engfracmech.2013.02.032, doi:10.1016/j.engfracmech.2013.02.032.

Broek, D., 1982. Elementary engineering fracture mechanics. Springer Dordrecht. doi:https://doi.org/10.1007/978-94-009-4333-9.

Chen, J., Yuan, H., 2002. A micro-mechanical damage model based on gradient plasticity: algorithms and applications. International Journal for Numerical Methods in Engineering 54, 399–420. URL: http://dx.doi.org/10.1002/nme.431, doi:10.1002/nme.431.

Chen, Y., Lorentz, E., Besson, J., 2020. Crack initiation and propagation in small-scale yielding using a nonlocal gtn model. International Journal of Plasticity 130, 102701. URL: https://www.sciencedirect.com/science/article/pii/S0749641919304085, doi:https://doi.org/10.1016/j.ijplas.2020.102701.

Cheng, S., Garnier, J., Marini, B., Madi, Y., Besson, J., 2025. Size and thickness effects on the ductile fracture toughness of a 316 l(n) austenitic stainless steel in as-received and aged conditions. Fatigue & Fracture of Engineering Materials & Structures 48, 3168–3184. URL: https://onlinelibrary.wiley.com/doi/abs/10.1111/ffe.14665, doi:https://doi.org/10.1111/ffe.14665, arXiv:https://onlinelibrary.wiley.com/doi/pdf/10.1111/ffe.14665.

Choisez, L., Ding, L., Marteleur, M., Idrissi, H., Pardoen, T., Jacques, P.J., 2020. High temperature rise dominated cracking mechanisms in ultra-ductile and tough titanium alloy. Nature Communications 11. URL: http://dx.doi.org/10.1038/s41467-020-15772-1, doi:10.1038/s41467-020-15772-1.

Chu, C.C., Needleman, A., 1980. Void Nucleation Effects in Biaxially Stretched Sheets. Journal of Engineering Materials and Technology 102, 249–256. URL: https://doi.org/10.1115/1.3224807, doi:10.1115/1.3224807.

Cotterell, B., Pardoen, T., Atkins, A., 2005. Measuring toughness and the cohesive stress–displacement relationship by the essential work of fracture concept. Engineering Fracture Mechanics 72, 827–848. URL: http://dx.doi.org/10.1016/j.engfracmech.2004.10.002, doi:10.1016/j.engfracmech.2004.10.002.

Das, R., 2022. Special issue: structural integrity of additively manufactured materials—developments in damage, fracture, fatigue and failure assessments. International Journal of Fracture 235, 1–2. URL: http://dx.doi.org/10.1007/s10704-022-00651-1, doi:10.1007/s10704-022-00651-1.

De Borst, R., Sluys, L., Muhlhaus, H., Pamin, J., 1993. Fundamental issues in finite element analyses of localization

of deformation. Engineering Computations 10, 99–121. URL: http://dx.doi.org/10.1108/eb023897, doi:10.1108/eb023897.

Depraetere, R., De Waele, W., Cauwels, M., Depover, T., Verbeken, K., Hertelé, S., 2023. Modeling of hydrogen-charged notched tensile tests of an x70 pipeline steel with a hydrogen-informed gurson model. Materials 16, 4839. URL: http://dx.doi.org/10.3390/ma16134839, doi:10.3390/ma16134839.

El-Naaman, S., Nielsen, K., 2013. Observations on mode i ductile tearing in sheet metals. European Journal of Mechanics - A/Solids 42, 54–62. URL: http://dx.doi.org/10.1016/j.euromechsol.2013.04.007, doi:10.1016/j.euromechsol.2013.04.007.

Elguedj, T., Bazilevs, Y., Calo, V., Hughes, T., 2008. and projection methods for nearly incompressible linear and non-linear elasticity and plasticity using higher-order nurbs elements. Computer Methods in Applied Mechanics and Engineering 197, 2732–2762. URL: http://dx.doi.org/10.1016/j.cma.2008.01.012, doi:10.1016/j.cma.2008.01.012.

Ernst, H., Paris, P., Landes, J., 1981. Estimations on J-Integral and Tearing Modulus T from a Single Specimen Test Record. ASTM International100 Barr Harbor Drive, PO Box C700, West Conshohocken, PA 19428-2959. pp. 476–502. URL: http://dx.doi.org/10.1520/STP28814S, doi:10.1520/stp28814s.

Fabrègue, D., Pardoen, T., 2008. A constitutive model for elastoplastic solids containing primary and secondary voids. Journal of the Mechanics and Physics of Solids 56, 719–741. URL: http://dx.doi.org/10.1016/j.jmps.2007.07.008, doi:10.1016/j.jmps.2007.07.008.

Faleskog, J., Gao, X., Shih, C., 1998. Cell model for nonlinear fracture analysis - i. micromechanics calibration. International Journal of Fracture 89, 355–373. doi:10.1023/A:1007421420901.

Forest, S., 2009. Micromorphic approach for gradient elasticity, viscoplasticity, and damage. Journal of Engineering Mechanics 135, 117–131. doi:10.1061/(ASCE)0733-9399(2009)135:3(117).

Frómeta, D., Cuadrado, N., Rehrl, J., Suppan, C., Dieudonné, T., Dietsch, P., Calvo, J., Casellas, D., 2021. Microstructural effects on fracture toughness of ultra-high strength dual phase sheet steels. Materials Science and Engineering: A 802, 140631. URL: http://dx.doi.org/10.1016/j.msea.2020.140631, doi:10.1016/j.msea.2020.140631.

Gaffard, V., Gourgues-Lorenzon, A., Besson, J., 2005. High temperature creep flow and damage properties of 9cr1monbv steels: Base metal and weldment. Nuclear Engineering and Design 235, 2547–2562. URL: http://dx.doi.org/10.1016/j.nucengdes.2005.07.001, doi:10.1016/j.nucengdes.2005.07.001.

Gludovatz, B., Hohenwarter, A., Thurston, K.V.S., Bei, H., Wu, Z., George, E.P., Ritchie, R.O., 2016. Exceptional damage-tolerance of a medium-entropy alloy crconi at cryogenic temperatures. Nature Communications 7. URL: http://dx.doi.org/10.1038/ncomms10602, doi:10.1038/ncomms10602.

Gologanu, M., Leblond, J.B., Devaux, J., 1993. Approximate models for ductile metals containing non-spherical voids—case of axisymmetric prolate ellipsoidal cavities. Journal of the Mechanics and Physics of Solids 41, 1723–1754. URL: https://www.sciencedirect.com/science/article/pii/002250969390029F, doi:https://doi.org/10.1016/0022-5096(93)90029-F.

Gurson, A.L., 1977. Continuum theory of ductile rupture by void nucleation and growth: Part i—yield criteria and flow rules for porous ductile media. Journal of Engineering Materials and Technology 99, 2–15. URL: http://dx.doi.org/10.1115/1.3443401, doi:10.1115/1.3443401.

Hilhorst, A., Jacques, P.J., Pardoen, T., 2023. Towards the best strength, ductility, and toughness combination: High entropy alloys are excellent, stainless steels are exceptional. Acta Materialia 260, 119280. URL: https://www.sciencedirect.com/science/article/pii/S1359645423006109, doi:https://doi.org/10.1016/j.actamat.2023.119280.

Hilhorst, A., Leclerc, J., Pardoen, T., Jacques, P.J., Noels, L., Nguyen, V.D., 2022. Ductile fracture of high entropy alloys: From the design of an experimental campaign to the development of a micromechanics-based modeling framework. Engineering Fracture Mechanics 275, 108844. URL: https://www.sciencedirect.com/science/article/pii/S0013794422005628, doi:https://doi.org/10.1016/j.engfracmech.2022.108844.

Hill, R., 1948. A theory of the yielding and plastic flow of anisotropic metals. Proceedings of the Royal Society of London. Series A. Mathematical and Physical Sciences 193, 281–297.

Hütter, G., Linse, T., Mühlich, U., Kuna, M., 2013a. Simulation of ductile crack initiation and propagation by means of a non-local gurson-model. International Journal of Solids and Structures 50, 662–671. URL: http://dx.doi.org/10.1016/j.ijsolstr.2012.10.031, doi:10.1016/j.ijsolstr.2012.10.031.

Hütter, G., Linse, T., Roth, S., Mühlich, U., Kuna, M., 2013b. A modeling approach for the complete ductile–brittle transition region: cohesive zone in combination with a non-local gurson-model. International Journal of Fracture 185, 129–153. URL: http://dx.doi.org/10.1007/s10704-013-9914-4, doi:10.1007/s10704-013-9914-4.

Håkansson, P., Wallin, M., Ristinmaa, M., 2006. Thermomechanical response of non-local porous material. International Journal of Plasticity 22, 2066–2090. URL: http://dx.doi.org/10.1016/j.ijplas.2005.08.003, doi:10.1016/j.ijplas.2005.08.003.

Ismail, K., Perlade, A., Jacques, P.J., Pardoen, T., 2021. Outstanding cracking resistance of fibrous dual phase steels. Acta Materialia 207, 116700. URL: http://dx.doi.org/10.1016/j.actamat.2021.116700, doi:10.1016/j.actamat.2021.116700.

Jirásek, M., 1998. Nonlocal models for damage and fracture: Comparison of approaches. International Journal of Solids and Structures 35, 4133–4145. URL: http://dx.doi.org/10.1016/S0020-7683(97)00306-5, doi:10.1016/s0020-7683(97)00306-5.

Kaniadakis, A., Nguyen, V.D., Besson, J., Pardoen, T., 2025. Strain hardening effect on ductile tearing under small scale yielding plane strain conditions. Journal of the Mechanics and Physics of Solids , 106171URL: http://dx.doi.org/10.1016/j.jmps.2025.106171, doi:10.1016/j.jmps.2025.106171.

Kim, J., Gao, X., Srivatsan, T.S., 2004. Modeling of void growth in ductile solids: effects of stress triaxiality and initial porosity. Engineering Fracture Mechanics 71, 379–400. URL: http://dx.doi.org/10.1016/S0013-7944(03)00114-0, doi:10.1016/s0013-7944(03)00114-0.

Kong, X., Helfen, L., Hurst, M., Hänschke, D., Missoum-Benziane, D., Besson, J., Baumbach, T., Morgeneyer, T.F., 2022. 3d in situ study of damage during a 'shear to tension' load path change in an aluminium alloy. Acta Materialia 231, 117842. URL: http://dx.doi.org/10.1016/j.actamat.2022.117842, doi:10.1016/j.actamat.2022.117842.

Koplik, J., Needleman, A., 1988. Void growth and coalescence in porous plastic solids. International Journal of Solids and Structures 24, 835–853. URL: http://dx.doi.org/10.1016/0020-7683(88)90051-0, doi:10.1016/0020-7683(88)90051-0.

Leblond, J.B., Perrin, G., Devaux, J., 1994. Bifurcation effects in ductile metals with nonlocal damage. Journal of Applied Mechanics 61, 236–242. URL: http://dx.doi.org/10.1115/1.2901435, doi:10.1115/1.2901435.

Leblond, J.B., Perrin, G., Devaux, J., 1995. An improved gurson-type model for hardenable ductile metals. European Journal of Mechanics A-solids 14, 499–527. URL: https://api.semanticscholar.org/CorpusID:118050919.

Lecarme, L., Maire, E., Kumar K.C., A., De Vleeschouwer, C., Jacques, L., Simar, A., Pardoen, T., 2014. Heterogenous void growth revealed by in situ 3-d x-ray microtomography using automatic cavity tracking. Acta Materialia 63, 130–139. URL: https://www.sciencedirect.com/science/article/pii/S1359645413007659, doi:https://doi.org/10.1016/j.actamat.2013.10.014.

Lin, M., Yu, H., Ding, Y., Wang, G., Olden, V., Alvaro, A., He, J., Zhang, Z., 2022. A predictive model unifying hydrogen enhanced plasticity and decohesion. Scripta Materialia 215, 114707. URL: http://dx.doi.org/10.1016/j.scriptamat.2022.114707, doi:10.1016/j.scriptamat.2022.114707.

Linse, T., Hütter, G., Kuna, M., 2012. Simulation of crack propagation using a gradient-enriched ductile damage model based on dilatational strain. Engineering Fracture Mechanics 95, 13–28. URL: http://dx.doi.org/10.1016/j.engfracmech.2012.07.004, doi:10.1016/j.engfracmech.2012.07.004.

Lopes Pinto, D., El Ouazani Tuhami, A., Osipov, N., Madi, Y., Besson, J., 2024. Simulation of hydrogen embrittlement of steel using mixed nonlocal finite elements. European Journal of Mechanics - A/Solids 104, 105116. URL: http://dx.doi.org/10.1016/j.euromechsol.2023.105116, doi:10.1016/j.euromechsol.2023.105116.

Madou, K., Leblond, J.B., 2012a. A gurson-type criterion for porous ductile solids containing arbitrary ellipsoidal voids—i: Limit-analysis of some representative cell. Journal of the Mechanics and Physics of Solids 60,

1020–1036. URL: http://dx.doi.org/10.1016/j.jmps.2011.11.008, doi:10.1016/j.jmps.2011.11.008.

Madou, K., Leblond, J.B., 2012b. A gurson-type criterion for porous ductile solids containing arbitrary ellipsoidal voids—ii: Determination of yield criterion parameters. Journal of the Mechanics and Physics of Solids 60, 1037–1058. URL: http://dx.doi.org/10.1016/j.jmps.2012.01.010, doi:10.1016/j.jmps.2012.01.010.

Marteleur, M., Leclerc, J., Colla, M.S., Nguyen, V.D., Noels, L., Pardoen, T., 2021. Ductile fracture of high strength steels with morphological anisotropy, part i: Characterization, testing, and void nucleation law. Engineering Fracture Mechanics 244, 107569. URL: http://dx.doi.org/10.1016/j.engfracmech.2021.107569, doi:10.1016/j.engfracmech.2021.107569.

Morgeneyer, T., Besson, J., 2011. Flat to slant ductile fracture transition: Tomography examination and simulations using shear-controlled void nucleation. Scripta Materialia 65, 1002–1005. URL: http://dx.doi.org/10.1016/j.scriptamat.2011.09.004, doi:10.1016/j.scriptamat.2011.09.004.

Morin, L., Leblond, J.B., Benzerga, A.A., Kondo, D., 2016. A unified criterion for the growth and coalescence of microvoids. Journal of the Mechanics and Physics of Solids 97, 19–36. URL: http://dx.doi.org/10.1016/j.jmps.2016.01.013, doi:10.1016/j.jmps.2016.01.013.

Nahshon, K., Hutchinson, J., 2008. Modification of the gurson model for shear failure. European Journal of Mechanics - A/Solids 27, 1–17. URL: https://www.sciencedirect.com/science/article/pii/S0997753807000721, doi:https://doi.org/10.1016/j.euromechsol.2007.08.002.

Nguyen, V.D., Pardoen, T., 2025. A ductile fracture model accounting for plastic anisotropy and its application in ductile tearing of thin metallic plates. in preparation .

Nguyen, V.D., Pardoen, T., Noels, L., 2020. A nonlocal approach of ductile failure incorporating void growth, internal necking, and shear dominated coalescence mechanisms. Journal of the Mechanics and Physics of Solids 137, 103891. URL: https://www.sciencedirect.com/science/article/pii/S0022509619309275, doi:https://doi.org/10.1016/j.jmps.2020.103891.

Onck, P., van der Giessen, E., 1998. Micromechanics of creep fracture: simulation of intergranular crack growth. Computational Materials Science 13, 90–102. URL: http://dx.doi.org/10.1016/S0927-0256(98)00049-4, doi:10.1016/s0927-0256(98)00049-4.

Papasidero, J., Doquet, V., Mohr, D., 2015. Ductile fracture of aluminum 2024-t351 under proportional and non-proportional multi-axial loading: Bao–wierzbicki results revisited. International Journal of Solids and Structures 69–70, 459–474. URL: http://dx.doi.org/10.1016/j.ijsolstr.2015.05.006, doi:10.1016/j.ijsolstr.2015.05.006.

Pardoen, T., Hachez, F., Marchioni, B., Blyth, P., Atkins, A., 2004. Mode i fracture of sheet metal. Journal of the Mechanics and Physics of Solids 52, 423–452. URL: https://www.sciencedirect.com/science/article/pii/S0022509603000875, doi:https://doi.org/10.1016/S0022-5096(03)00087-5.

Pardoen, T., Hutchinson, J., 2000. An extended model for void growth and coalescence. Journal of the Mechanics and Physics of Solids 48, 2467–2512. URL: https://www.sciencedirect.com/science/article/pii/S0022509600000193, doi:https://doi.org/10.1016/S0022-5096(00)00019-3.

Pardoen, T., Hutchinson, J., 2003. Micromechanics-based model for trends in toughness of ductile metals. Acta Materialia 51, 133–148. URL: https://www.sciencedirect.com/science/article/pii/S1359645402003865, doi:https://doi.org/10.1016/S1359-6454(02)00386-5.

Pardoen, T., Marchal, Y., Delannay, F., 1999. Thickness dependence of cracking resistance in thin aluminium plates. Journal of the Mechanics and Physics of Solids 47, 2093–2123. URL: http://dx.doi.org/10.1016/S0022-5096(99)00011-3, doi:10.1016/s0022-5096(99)00011-3.

Pardoen, T., Scheyvaerts, F., Simar, A., Tekoğlu, C., Onck, P.R., 2010. Multiscale modeling of ductile failure in metallic alloys. Comptes Rendus. Physique 11, 326–345. URL: http://dx.doi.org/10.1016/j.crhy.2010.07.012, doi:10.1016/j.crhy.2010.07.012.

Peerlings, R., Borst, de, R., Brekelmans, W., Geers, M., 1998. Gradient-enhanced damage modelling of concrete fracture. Mechanics of Cohesive-Frictional Materials 3, 323–342. doi:10.1002/(SICI)1099-1484(1998100)3:4<323::AID-CFM51>3.0.CO;2-Z.

Peerlings, R., Geers, M., de Borst, R., Brekelmans, W., 2001. A critical comparison of nonlocal and gradient-enhanced softening continua. International Journal of Solids and Structures 38, 7723–7746. URL: http://dx.doi.org/10.1016/S0020-7683(01)00087-7, doi:10.1016/s0020-7683(01)00087-7.

Peerlings, R.H.J., de Borst, R., Brekelmans, W.A.M., de Vree, J.H.P., 1996. Gradient enhanced damage for quasi-brittle materials. International Journal for Numerical Methods in Engineering 39, 3391–3403. URL: http://dx.doi.org/10.1002/(SICI)1097-0207(19961015)39:19<3391::AID-NME7>3.0.CO;2-D, doi:10.1002/(sici)1097-0207(19961015)39:19<3391::aid-nme7>3.0.co;2-d.

Petti, J.P., Dodds, R.H., 2005. Ductile tearing and discrete void effects on cleavage fracture under small-scale yielding conditions. International Journal of Solids and Structures 42, 3655–3676. URL: http://dx.doi.org/10.1016/j.ijsolstr.2004.11.015, doi:10.1016/j.ijsolstr.2004.11.015.

Pineau, A., Benzerga, A., Pardoen, T., 2016. Failure of metals i: Brittle and ductile fracture. Acta Materialia 107, 424–483. URL: https://www.sciencedirect.com/science/article/pii/S1359645415301403, doi:https://doi.org/10.1016/j.actamat.2015.12.034.

Ramaswamy, S., Aravas, N., 1998. Finite element implementation of gradient plasticity models part ii: Gradient-dependent evolution equations. Computer Methods in Applied Mechanics and Engineering 163, 33–53. URL: http://dx.doi.org/10.1016/S0045-7825(98)00027-9, doi:10.1016/s0045-7825(98)00027-9.

Reusch, F., Hortig, C., Svendsen, B., 2008. Nonlocal modeling and simulation of ductile damage and failure in metal matrix composites. Journal of Engineering Materials and Technology 130. URL: http://dx.doi.org/10.1115/1.2840967, doi:10.1115/1.2840967.

Reusch, F., Svendsen, B., Klingbeil, D., 2003a. Local and non-local gurson-based ductile damage and failure modelling at large deformation. European Journal of Mechanics - A/Solids 22, 779–792. URL: http://dx.doi.org/10.1016/S0997-7538(03)00070-6, doi:10.1016/s0997-7538(03)00070-6.

Reusch, F., Svendsen, B., Klingbeil, D., 2003b. A non-local extension of gurson-based ductile damage modeling. Computational Materials Science 26, 219–229. URL: http://dx.doi.org/10.1016/S0927-0256(02)00402-0, doi:10.1016/s0927-0256(02)00402-0.

Rice, J.R., Paris, P.C., Merkle, J.G., 1973. Some Further Results of J-Integral Analysis and Estimates. ASTM International100 Barr Harbor Drive, PO Box C700, West Conshohocken, PA 19428-2959. pp. 231–245. URL: http://dx.doi.org/10.1520/STP49643S, doi:10.1520/stp49643s.

Rivalin, F., Besson, J., Pineau, A., Di Fant, M., 2001. Ductile tearing of pipeline-steel wide plates. Engineering Fracture Mechanics 68, 347–364. URL: http://dx.doi.org/10.1016/S0013-7944(00)00108-9, doi:10.1016/s0013-7944(00)00108-9.

Roubaud, F., Morin, L., Remmal, A., Marie, S., Leblond, J.B., 2024. A gurson-type layer model for ductile porous solids containing ellipsoidal voids with isotropic and kinematic hardening. European Journal of Mechanics - A/Solids 104, 105114. URL: http://dx.doi.org/10.1016/j.euromechsol.2023.105114, doi:10.1016/j.euromechsol.2023.105114.

Ruggieri, C., Dodds, R.H., 2018. A local approach to cleavage fracture modeling: An overview of progress and challenges for engineering applications. Engineering Fracture Mechanics 187, 381–403. URL: http://dx.doi.org/10.1016/j.engfracmech.2017.12.021, doi:10.1016/j.engfracmech.2017.12.021.

Samal, M., Seidenfuss, M., Roos, E., Dutta, B., Kushwaha, H., 2008. Experimental and numerical investigation of ductile-to-brittle transition in a pressure vessel steel. Materials Science and Engineering: A 496, 25–35. URL: http://dx.doi.org/10.1016/j.msea.2008.06.046, doi:10.1016/j.msea.2008.06.046.

Scheyvaerts, F., Pardoen, T., Onck, P., 2010. A new model for void coalescence by internal necking. International Journal of Damage Mechanics 19, 126 – 95. URL: https://api.semanticscholar.org/CorpusID:137294886.

Shahani, A., Rastegar, M., Botshekanan Dehkordi, M., Moayeri Kashani, H., 2010. Experimental and numerical investigation of thickness effect on ductile fracture toughness of steel alloy sheets. Engineering Fracture Mechanics 77, 646–659. URL: http://dx.doi.org/10.1016/j.engfracmech.2009.12.017, doi:10.1016/j.engfracmech.2009.12.017.

Shinohara, Y., Madi, Y., Besson, J., 2016. Anisotropic ductile failure of a high-strength line pipe steel. International Journal of Fracture 197, 127–145. URL: http://dx.doi.org/10.1007/s10704-015-0054-X, doi:10.

1007/s10704-015-0054-x.

Siegmund, T., Brocks, W., 2000. A numerical study on the correlation between the work of separation and the dissipation rate in ductile fracture. Engineering Fracture Mechanics 67, 139–154. URL: http://dx.doi.org/10.1016/S0013-7944(00)00054-0, doi:10.1016/s0013-7944(00)00054-0.

Tanguy, B., Bouchet, C., Bugat, S., Besson, J., 2006. Local approach to fracture based prediction of the δt56j and shifts due to irradiation for an a508 pressure vessel steel. Engineering Fracture Mechanics 73, 191–206. URL: http://dx.doi.org/10.1016/j.engfracmech.2005.05.006, doi:10.1016/j.engfracmech.2005.05.006.

Thaulow, C., Østby, E., Nyhus, B., Zhang, Z.L., Skallerud, B., 2004. Constraint correction of high strength steel. Engineering Fracture Mechanics 71, 2417–2433. URL: http://dx.doi.org/10.1016/j.engfracmech.2004.01.003, doi:10.1016/j.engfracmech.2004.01.003.

Tuhami, A.E.O., Feld-Payet, S., Quilici, S., Osipov, N., Besson, J., 2022. A two characteristic length nonlocal gtn model: Application to cup–cone and slant fracture. Mechanics of Materials 171, 104350. URL: http://dx.doi.org/10.1016/j.mechmat.2022.104350, doi:10.1016/j.mechmat.2022.104350.

Tvergaard, V., 1998. Interaction of very small voids with larger voids. International Journal of Solids and Structures 35, 3989–4000. URL: http://dx.doi.org/10.1016/S0020-7683(97)00254-0, doi:10.1016/s0020-7683(97)00254-0.

Tvergaard, V., 2001. Crack growth predictions by cohesive zone model for ductile fracture. Journal of the Mechanics and Physics of Solids 49, 2191–2207. URL: http://dx.doi.org/10.1016/S0022-5096(01)00030-8, doi:10.1016/s0022-5096(01)00030-8.

Tvergaard, V., Legarth, B.N., 2004. Effect of plastic anisotropy on crack growth resistance under mode 1 loading. International Journal of Fracture 130, 411–425. URL: http://dx.doi.org/10.1023/B:FRAC.0000049498.15818.33, doi:10.1023/b:frac.0000049498.15818.33.

Tvergaard, V., Needleman, A., 1984. Analysis of the cup-cone fracture in a round tensile bar. Acta Metallurgica 32, 157–169. URL: https://www.sciencedirect.com/science/article/pii/000161608490213X, doi:https://doi.org/10.1016/0001-6160(84)90213-X.

Tvergaard, V., Needleman, A., 1995. Effects of nonlocal damage in porous plastic solids. International Journal of Solids and Structures 32, 1063–1077. URL: http://dx.doi.org/10.1016/0020-7683(94)00185-Y, doi:10.1016/0020-7683(94)00185-y.

Van Der Giessen, E., Onck, P., Van Der Burg, M., 1997. Some effects of random microstructural variations on creep rupture. Engineering Fracture Mechanics 57, 205–226. URL: http://dx.doi.org/10.1016/S0013-7944(97)00009-X, doi:10.1016/s0013-7944(97)00009-x.

Xia, L., 1995. A computational approach to ductile crack growth under large scale yielding conditions. Journal of the Mechanics and Physics of Solids 43, 389–413. URL: http://dx.doi.org/10.1016/0022-5096(94)00069-H, doi:10.1016/0022-5096(94)00069-h.

Xia, L., Shih, C., 1996. Ductile crack growth—iii. transition to cleavage fracture incorporating statistics. Journal of the Mechanics and Physics of Solids 44, 603–639. URL: http://dx.doi.org/10.1016/0022-5096(95)00086-0, doi:10.1016/0022-5096(95)00086-0.

Xiong, Z., Jacques, P.J., Perlade, A., Pardoen, T., 2018. Ductile and intergranular brittle fracture in a two-step quenching and partitioning steel. Scripta Materialia 157, 6–9. URL: http://dx.doi.org/10.1016/j.scriptamat.2018.07.030, doi:10.1016/j.scriptamat.2018.07.030.

Yin, C., Terentyev, D., Zhang, T., Nogami, S., Antusch, S., Chang, C.C., Petrov, R.H., Pardoen, T., 2021. Ductile to brittle transition temperature of advanced tungsten alloys for nuclear fusion applications deduced by miniaturized three-point bending tests. International Journal of Refractory Metals and Hard Materials 95, 105464. URL: http://dx.doi.org/10.1016/j.ijrmhm.2020.105464, doi:10.1016/j.ijrmhm.2020.105464.

Yu, H., Olsen, J.S., Alvaro, A., Olden, V., He, J., Zhang, Z., 2016. A uniform hydrogen degradation law for high strength steels. Engineering Fracture Mechanics 157, 56–71. URL: http://dx.doi.org/10.1016/j.engfracmech.2016.02.001, doi:10.1016/j.engfracmech.2016.02.001.

Zhang, Y., Lorentz, E., Besson, J., 2018. Ductile damage modelling with locking-free regularised gtn model. International Journal for Numerical Methods in Engineering 113, 1871–1903. URL: https://onlinelibrary.wiley.com/doi/abs/10.1002/nme.5722, doi:https://doi.org/10.1002/

nme.5722, arXiv:https://onlinelibrary.wiley.com/doi/pdf/10.1002/nme.5722.

Zhang, Z., Thaulow, C., Ødegård, J., 2000. A complete gurson model approach for ductile fracture. Engineering Fracture Mechanics 67, 155–168. URL: http://dx.doi.org/10.1016/S0013-7944(00)00055-2, doi:10.1016/s0013-7944(00)00055-2.

Zinkle, S.J., Busby, J.T., 2009. Structural materials for fission & fusion energy. Materials Today 12, 12–19. URL: http://dx.doi.org/10.1016/S1369-7021(09)70294-9, doi:10.1016/s1369-7021(09)70294-9.

Zybell, L., Hütter, G., Linse, T., Mühlich, U., Kuna, M., 2014. Size effects in ductile failure of porous materials containing two populations of voids. European Journal of Mechanics - A/Solids 45, 8–19. URL: http://dx.doi.org/10.1016/j.euromechsol.2013.11.006, doi:10.1016/j.euromechsol.2013.11.006.